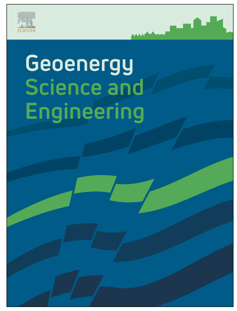


# Numerical modeling of temperature-reporting nanoparticle tracer for fractured geothermal reservoir characterization

Guoqiang Yan, PalOstebo Andersen, Yangyang Qiao, Dimitrios Georgios Hatzignatiou, Fabian Nitschke, Laura Spitzmuller, Thomas Kohl

PII: S2949-8910(24)00157-X

DOI: https://doi.org/10.1016/j.geoen.2024.212787

Reference: GEOEN 212787

To appear in: *Geoenergy Science and Engineering*

Received Date: 15 January 2024

Revised Date: 18 March 2024

Accepted Date: 25 March 2024

# Numerical modeling of temperature-reporting nanoparticle tracer for fractured geothermal reservoir characterization

**Guoqiang Yan[1], Pål Østebø Andersen[2], Yangyang Qiao[1*], Dimitrios Georgios Hatzignatiou[3], Fabian Nitschke[1], Laura Spitzmüller[1], Thomas Kohl[1]**

[1]Institute of Applied Geosciences, Karlsruhe Institute of Technology, Karlsruhe 76131, Germany
[2]Department of Energy Resources, University of Stavanger, Stavanger 4068, Norway
[3]Department of Petroleum Engineering, University of Houston, Houston TX 77204, USA

Corresponding author: Yangyang Qiao (yangyang.qiao@kit.edu)



## Highlights

- Temperature-reporting nanoparticle tracer tests are numerically implemented in a three-dimensional fractured geothermal reservoir.
- The working mechanisms of the temperature-reporting nanoparticle tracers are illustrated through field simulations using a proposed modeling approach.
- Our proposed analysis curves can provide responses to the reservoir temperature distribution as well as geological and thermal heterogeneities based on the tracer breakthrough data.

**Abstract**

Information on the temperature distribution of subsurface reservoirs is essential for geothermal energy development. One of the promising tools to detect the reservoir temperature distribution is temperature-reporting nanoparticle tracers whose functionality has been extensively investigated in both theoretical and experimental ways in the last decade. However, most related studies were limited to simplified geometries and ignored the dynamic interplays of fluid flow, heat transfer, transport and reaction of the temperature-reporting nanoparticle tracer. The response behavior and working mechanisms of such nanotracers in a realistic three-dimensional system still have not been fully revealed through a systematic study. In this work, we develop a numerical modeling approach to simulate field implementation of these nanotracers in a fractured geothermal reservoir. This study aims to evaluate whether the injection of multiple temperature-reporting nanoparticle tracers with different thresholds can be used to estimate the temperature distribution and provide information on the thermal and geological heterogeneities. Several scenarios have been investigated for the geothermal reservoir including homogeneous and non-homogeneous cases (e.g., thermal and geological heterogeneities). Our obtained results from the nanotracer breakthrough curves show that the deviation temperatures in peak concentration values provide an upper limit of the lowest temperature and precise highest temperature for the reservoir temperature range. The deviation temperature of the peak arrival time curve accurately estimates the highest temperature along the main streamlines between the wells. The proposed analysis curves based on the nanotracer breakthrough data were visibly affected by geological heterogeneities including their conductivities and orientations as well as thermal heterogeneities in the geothermal reservoir.

**Keywords**: nanoparticle; tracer; temperature-reporting; geothermal; reservoir characterization; tracer breakthrough curve

## 1 Introduction

Geothermal energy is a clean, renewable and sustainable alternative to traditional energy sources of fossil fuels for direct heat utilization and electricity generation (Moeck, 2014). According to the World Geothermal Congress (2023), a total of 1,476 PJ (410 TWh) of geothermal energy was used globally in 2022, a 44% increase from 2020, with geothermal heating and cooling of buildings accounting for about 79% of the total. While major geothermal systems are restricted to structurally dynamic or volcanically active regions (Lund et al., 2008; J. W. Tester et al., 1989), enhanced geothermal system (EGS) technology radically expands the global geothermal potential through hydraulic/thermal/chemical stimulation on target reservoirs to enhance permeability and fluid flow rate, in impermeable and low heat flow regions. Nonetheless, to improve the economic benefits and reduce investment risk in geothermal projects, reservoir characterization is particularly needed to evaluate subsurface heat/energy utilization capabilities in terms of geothermal power generation, as well as the management, maintenance and sustainability of operational plants (Domra Kana et al., 2015; S.-M. Lu, 2018; Olasolo et al., 2016). In general, geothermal reservoir characterization includes assessing reservoir conditions such as estimating temperature profiles (i.e., temperature range and distribution), surveying well-to-well or inter-well connectivity (Dashti et al., 2023) and extrapolating the volume of the fractured zones (B. Sanjuan et al., 2006). Among all reservoir characteristics, temperature profiles are critical for geothermal energy exploration and assessment in the geothermal reservoir (re-)siting step, as well as for evaluating reservoir thermal performance (e.g., thermal breakthrough prediction due to reinjection of cooled geothermal fluid) and adjusting production strategy in the production step. Nevertheless, the reliable and accurate measurement or estimation of temperature profiles throughout the lifecycle of geothermal energy development has always been a major, complex and difficult challenge for geothermal reservoirs (Frey et al., 2022).

Common methods to measure or estimate temperature profiles include wellbore measurements, geothermometers, analytical/numerical models and tracer tests. Temperature measurements at or near the wellbore do not provide temperature distributions between injection and production wells due to the limited space of the wellbore in the geothermal reservoir. Since the introduction of geothermometers in the 1960s, geothermometer technology has continued to advance in-situ temperature measurements by evaluating sensitive parameters with respect to the chemical equilibrium of fluids and reservoir rocks (e.g., aluminum concentration, pH, vapor loss, etc.) (Fournier & Rowe, 1966; Nitschke et al., 2017; B. Sanjuan et al., 2014; Ystroem et al., 2020). However, the spatial distribution of reservoir temperature is still unknown using geothermometers. Gringarten et al. (1975) presented an analytical solution for temperature determination, based on pure fluid flow and heat transfer in a hot-dry rock reservoir with infinite, equidistant and parallel fractures. Following that, many researchers (P. Cheng, 1979; A. H.-D. Cheng et al., 2001; Fox et al., 2016; Tang et al., 2020; Wilkins et al., 2021) continued to develop analytical solutions and numerical simulators to predict the temperature distribution in fractured geothermal reservoirs.

Nevertheless, with the large uncertainties in the geometry of fractures (e.g. aperture, scale, spacing and network) and heat transfer of unfractured zones, their results can only serve as references in practice, although these results are sometimes informative. To compensate for such shortcomings, conservative solute tracers (Erol et al., 2022; Pollack et al., 2021; Robinson, 1985; Robinson & Tester, 1984; Williams et al., 2010; Xu et al., 2022) and adsorbing solute tracers (C. Dean et al., 2012; Hawkins et al., 2018; Leecaster et al., 2012; Williams et al., 2013) which are able to adhere to the fracture surface were used in field tests to identify key geometry properties (i.e., heat transfer surface area, fracture aperture, etc.) of geothermal reservoirs, assisted by fitting analytical solutions of tracer transportation. Utilizing the obtained geometry properties, the reservoir temperature distribution is roughly estimated by using analytical or numerical models for heat transfer (Robinson, 1985; Williams et al., 2013). In addition, temperature-dependent degrading (Arrhenius reaction kinetics) solute tracers are proposed to infer the average reservoir temperature in fields by analytically fitting the tracers' degradation characteristics (Plummer et al., 2010; Plummer et al., 2011; P. E. Rose, 1994; J. W. Tester et al., 1987). It should be noted that the reaction rates of such kind of tracers vary with the environmental temperature and this method only provides the average reservoir temperatures without spatial temperature information in a single test. Although solute tracers have been used in many fields for temperature estimation in fractured geothermal reservoirs, the combined effects of their diffusion and interaction with reservoir rocks as well as highly mineralized reservoir fluids give rise to less reliable tracer tests due to the high mass loss, low detectability and collectability of the solute tracers (Aydin et al., 2022; Rudolph et al., 2020; Vitorge et al., 2014).

To eliminate deficiencies in solute tracer tests, nanoparticles with controllable size, structure and physical and chemical properties are utilized to measure or estimate temperature profiles in geothermal reservoirs by different transport (e.g., low diffusion) and working mechanisms from solute tracer (Divine & McDonnell, 2005; X.-Z. Kong et al., 2018; Redden et al., 2010). One kind of tracer named 'temperature-sensitive nanotracer' is attractive and utilized to detect thermal drawdown and average temperature by quantifying the extent of tracer degradation. The degradation starts from a certain temperature threshold and its rate is influenced by the environmental temperature (Axelsson et al., 2001; Nottebohm et al., 2012; Robinson et al., 1988)). Many theoretical and experimental studies have been done to investigate the performance behavior of temperature-sensitive nanotracers. For example, theoretically, Ames et al. (2015) used the analytical solution of tracer distribution in the one-dimensional model to inversely predict the thermal drawdown. However, their work does not consider the dynamic interplays of heat transfer, fluid flow, transport and reaction of the nanotracer. In addition, Alaskar et al. (2015) analytically and experimentally exhibited the prospects of temperature-sensitive nanotracers for forecasting the thermal drawdown. In 2021, a field demonstration of temperature-sensitive nanotracers by Hawkins et al. (2021) showed that the estimated effective inter-well reservoir temperatures have an error of less than 5°C from the true values. However, the above studies have not demonstrated how inter-well test results from temperature-reporting nanotracers are related to geological heterogeneities, temperature distributions and well positioning.

Different from the degradation principle of a temperature-sensitive nanotracer after reaching the temperature threshold, a novel tracer called a ‘temperature-reporting nanoparticle tracer’ (also ‘temperature-reporting nanotracers’ for simplicity) can be quickly, fully and irreversibly converted when the environmental temperature reaches a certain threshold, are being studied to characterize the temperature distribution of geothermal reservoirs (Puddu et al., 2016; Rudolph et al., 2020). It was Williams et al. (2010) and Alaskar et al. (2011) who first introduced a dye-release mechanism, wherein encapsulated dyes are released from the nanotracer upon reaching a specific temperature threshold. France et al. studied polymer microcapsules encapsulating dyes that release dyes at a certain temperature threshold. Alaskar et al. (2015) experimentally developed irreversible thermochromic microspheres and dye-attached silica nanoparticles and exhibited their prospect as temperature sensors for forecasting the thermal drawdown analytically and experimentally. Puddu et al. (2016) invented the submicrometer-sized particle, demonstrating for the first time the feasibility of using nucleic acid damage quantitatively to measure temperature. Rudolph et al. (2020) conducted experiments to develop temperature-reporting nanotracers by silica particles synthesized with the core-shell-hull layers. The outer dye in the nanotracer is released irreversibly once the environmental temperature is above its thresholds, giving rise to changes in the structure of the developed nanoparticle tracers. Nevertheless, these works primarily focused on concept development, laboratory research and analytical analysis.

The motivation of this work is to investigate whether temperature-reporting nanotracers can be used for the characterization of 3D geothermal reservoirs related to reservoir temperature distribution prediction, and provide methodologies that when applied enable the development and exploitation of geothermal energy resources. Presently, there have not been theoretical studies to reveal the working behavior of the temperature-reporting nanotracers, nor have these nanotracers been tested in realistic 3D geothermal reservoirs. The mutual interplay among fluid flow, heat transfer, transport and reaction of the temperature-reporting nanotracers and reservoir heterogeneity necessitates a detailed investigation. In addition, how to design and implement a temperature-reporting nanotracer test in geothermal reservoirs is also questionable. Therefore, numerical simulation can be utilized as a useful approach to shed light on these issues and help us gain insight into the potential of implementing temperature-reporting nanotracers in the field.

The goal of the current work is to study the working mechanisms (i.e., transport, reaction, distribution and resulting concentration breakthrough curves) of temperature-reporting nanotracers in synthetic but typical 3D fractured geothermal reservoirs as well as their performance in the detection of reservoir temperature distributions through analyzing its breakthrough data. To achieve that, a numerical modeling approach is developed for the reaction of temperature-reporting nanotracers. The novelty of this work is the application of a new analysis method based on the peak information of nanotracer breakthrough curves proposed to estimate the temperature along the tested injection-production positions and reservoir temperature range of the fractured geothermal reservoir.

The paper is organized as follows. We first present the employed methodology for modeling temperature-reporting nanotracer transport in fractured geothermal reservoirs, including the reaction mechanism of temperature-reporting nanotracers and numerical modeling approaches. Secondly, the potential of temperature-reporting nanotracers in fractured geothermal reservoirs and the effect of well configuration on the temperature-reporting nanotracers' responses are evaluated in a homogeneous model. Finally, the thermal distributions (i.e., different temperature gradients and regional thermal anomalies) and effects of reservoir heterogeneity (i.e., embedded by inclined zones) within the geothermal reservoir are studied.

## 2 Materials and Methods

A liquid solution is injected into the fractured geothermal reservoir through the injection well for a short period, followed by pure water injection the rest of the time. The solution is a mixture of water and temperature-reporting nanotracers with different temperature thresholds. The temperature-reporting nanoparticle nanotracers being simulated are representative of silica particles synthesized with core-shell-hull layers developed to characterize temperature distribution when the environmental temperature reaches its threshold (Rudolph et al. (2020)). The nanotracer breakthrough data are monitored in the production well during the injection process.

The modeled physical and chemical processes consist of fluid flow, heat transfer, transport and the reaction of temperature-reporting nanotracers in the reservoir. The numerical models for simulating fully coupled processes of fluid flow, heat transfer, transport and reaction for temperature-reporting nanotracer are developed for the first time and implemented in the finite element simulator-PorousFlow module (Wilkins et al., 2021) within the MOOSE framework (Permann et al., 2020). The relevant equations are described in detail below. The numerical algorithm and validation of fully coupled processes among fluid flow, heat transfer, transport and reaction for temperature-reporting nanoparticle tracers are given in **Appendices I** and **II**, respectively.

## 2.1 Governing Equations

### 2.1.1 Fluid Flow and Heat Transfer

Firstly, the fluid mass balance equation (Cacace & Jacquey, 2017) for compressible and liquid-phase water flow in porous media is written as:

$$\frac{\partial(\phi\rho_w)}{\partial t} + \nabla \cdot (\rho_w \boldsymbol{u_w}) - Q_w = 0 \quad (1)$$

where $\phi$ is the porosity (-) of the porous medium, $t$ represents time (s), the subscript $w$ refers to water, $p_w$ is the pressure (Pa), $T$ is the temperature (K), $\rho_w = \rho_w(p_w, T)$ is the water density (kg·m$^{-3}$) as a function of pressure and temperature, $\boldsymbol{u_w}$ is the Darcy velocity (m·s$^{-1}$) and $Q_w$ is the water mass source (kg·m$^{-3}$·s$^{-1}$).

The Darcy velocity $\boldsymbol{u_w}$ (Qiao et al., 2018) is given as:

$$\boldsymbol{u_w} = \frac{k}{\mu_w}(-\nabla p_w + \rho_w \boldsymbol{g}) \quad (2)$$

where $k$ is the reservoir permeability (m$^2$), $\mu_w = \mu_w(p_w, T)$ refers to the water viscosity (Pa s) as a function of pressure and temperature, and $\boldsymbol{g}$ is the gravitational acceleration (m·s$^{-2}$).

Secondly, the heat transfer equation (T. Kohl & Rybach, 1996) for both solid and water in the porous media is written as:

$$\left[\phi c_{p,w}\rho_w + (1-\phi)c_{p,s}\rho_s\right]\frac{\partial T}{\partial t} - [\phi\lambda_w + (1-\phi)\lambda_s]\,\nabla^2 T + \rho_w c_{p,w}\boldsymbol{u_w}\nabla T - Q_T = 0 \quad (3)$$

where the four terms on the left side individually represent a transient variation of temperature, heat conduction, heat convection and heat source. The subscript $s$ represents the solid phase, $c_{p,w}$

and $c_{p,s}$ are separately the specific heat capacity of water and solid (J·m$^{-3}$·K$^{-1}$), $\rho_s$ denotes the solid density (kg·m$^{-3}$), $T$ is the temperature (K), $\lambda_w$ and $\lambda_s$ refer to the heat conductivity of the water and solid (W·m$^{-1}$·K$^{-1}$) and $Q_T$ is the heat source (W·m$^{-3}$).

### 2.1.2 Reaction and Transport of Temperature-reporting Nanoparticle Tracers

#### (a) Reaction Process

Figure 1 illustrates the working mechanism for reporting temperature information of the temperature-reporting nanotracer which are silica particles synthesized with the core-shell-hull layers. Specifically, the hull melts/degrades, dyes are released and the structure of the developed tracer (reactant) changes when the environment temperature exceeds the temperature threshold of the temperature-reporting nanotracer. The product resulting from this temperature-dependent reaction is our research focus. The released dyes only act as indicators of the reaction completion degree in the lab, without directly reflecting temperature changes (Rudolph et al., 2020). In addition, dyes may interact with highly mineralized reservoir fluids and adsorb onto the reservoir rock. Therefore, in this study released dyes are not involved in the temperature reporting mechanism.

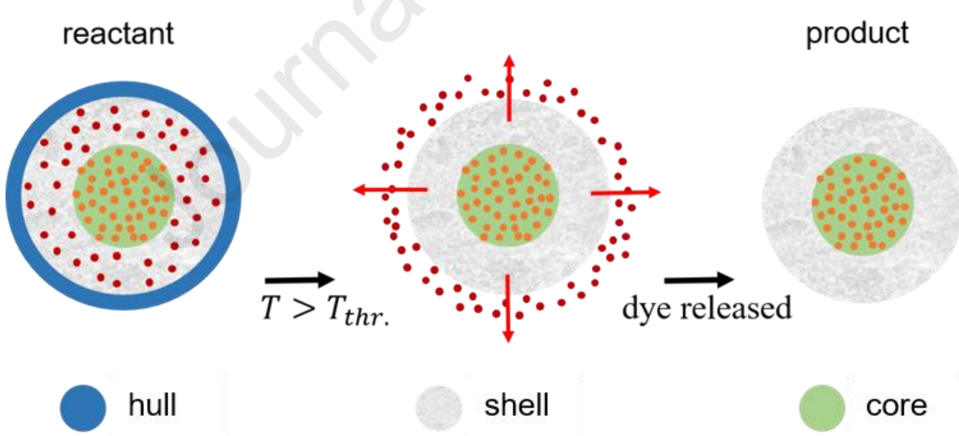


**Figure 1. Schematic representation of the working mechanism of temperature-reporting nanotracers: the dye released from the shell of the nanoparticles upon exceeding the temperature threshold (reproduced from Rudolph et al. (2020)).**

In the following, we present our numerical approach for simulating the temperature-reporting nanotracers reaction. Referring to Figure 1, the relevant reaction can be described as follows:

$$C_{T_{thre.}}^{reac.} \xrightarrow{T>T_{thre.}} C_{T_{thre.}}^{prod.} \qquad (4)$$

where $C_{T_{thre.}}^{reac.}$ denotes the concentration of reactant and $C_{T_{thre.}}^{prod.}$ is the corresponding product's concentration after the reaction. $T_{thre.}$ refers to the temperature threshold of the reactant.

**(b) Transport Process**

Each temperature-reporting nanotracer with a certain temperature threshold has a group of the two advection-diffusion equations (Shan & Pruess, 2005) for both reactant and product:

$$\frac{\partial C_{T_{thre.}}^{reac.}}{\partial t} - \nabla \cdot (\boldsymbol{D} \nabla C_{T_{thre.}}^{reac.}) + \nabla \cdot (\boldsymbol{u_w} C_{T_{thre.}}^{reac.}) - Q_{C_{T_{thre.}}^{reac.}} = 0 \tag{5}$$

$$\frac{\partial C_{T_{thre.}}^{prod.}}{\partial t} - \nabla \cdot (\boldsymbol{D} \nabla C_{T_{thre.}}^{prod.}) + \nabla \cdot (\boldsymbol{u_w} C_{T_{thre.}}^{prod.}) - Q_{C_{T_{thre.}}^{prod.}} = 0 \tag{6}$$

where $\boldsymbol{D}$ refers to the diffusion coefficient ($m^2 \cdot s^{-1}$), $\boldsymbol{u_w}$ is the Darcy velocity ($m \cdot s^{-1}$), $Q_{C_{T_{thre.}}^{reac.}}$ and $Q_{C_{T_{thre.}}^{prod.}}$ represent the mass source of reactant and product ($kg \cdot m^{-3} \cdot s^{-1}$), respectively. Here we assume that the nanotracers are well mixed with water as components of the liquid solution and the gravity segregation between water and nanotracer is ignored due to the low mass fraction ($<10^{-3}$) of nanotracers in the liquid. In addition, for simplicity we do not consider the deposition and aggregation of nanotracers during the flow process.

The detailed discretization and algorithm for solving the fully coupled processes of fluid flow, heat transfer, transport and reaction of temperature-reporting nanoparticle tracers are given in **Appendix I**.

## 2.2 Model Description and Input Data

Our model is inspired by a typical fractured reservoir setting such as Soultz-sous-Forêts EGS (Egert et al., 2020) which contains several irregularly distributed fractures. In this study, a highly permeable and thin reservoir is used to mimic a fracture ($\phi = 1$). We use the model settings illustrated in Figure 2 (a). The reservoir model consists of two types of 600 m thick rocks: an inner stimulated (called 'inner reservoir') and an outer non-stimulated reservoir (called 'outer reservoir'). Both are covered by low permeable caprock and underlain by a low permeable bedrock. The ground surface temperature is assumed to be 20°C and the initial geothermal gradient is 0.05°C·$m^{-1}$. The initial pressure distribution is based on the hydrostatic gradient. For the model boundary conditions, we use a constrained (initial) pressure and (initial) temperature at the top (2 km depth) and a constant (initial) temperature at the bottom (3.6 km depth). The other facies of the model are set with closed boundaries.

We assume two wells into the inner reservoir, each having three possible injection/production points, thus leading to nine model configurations with different fluid/tracer schemes. The reservoir depth is between -2.5 km to -3.1 km and extending -0.5 km to 0.5 km horizontally. The unstructured mesh consisting of tetrahedral elements was created by the GMSH software (Geuzaine & Remacle, 2009). The element size differs between 1 m (around the wells) and 400 m (close to the boundaries) with a typical element size of 25 m inside the inner reservoir. Mesh sensitivity analysis is shown in **Appendix III**. The physical properties of rock and fluid are summarized in **Table 1** and **Table 2**, respectively.

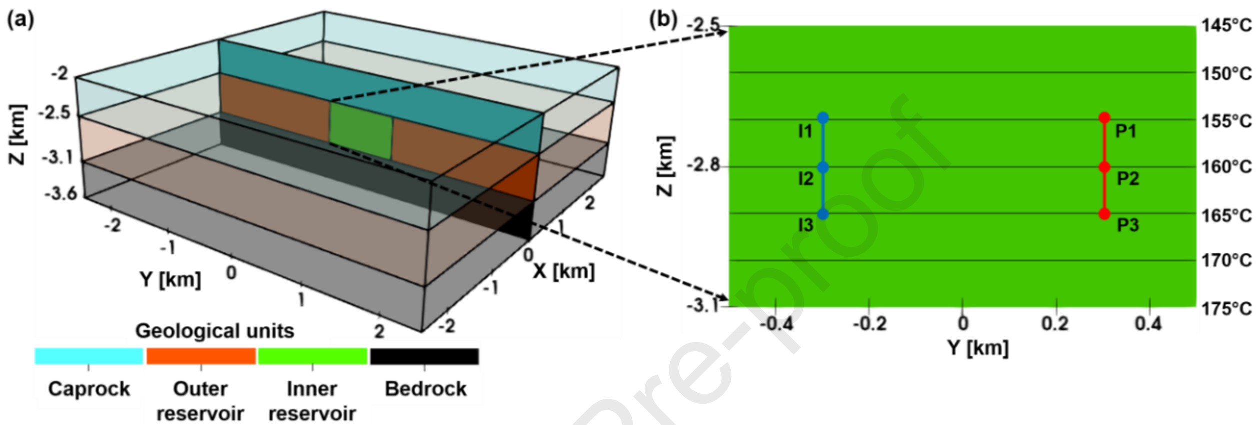


**Figure 2. The reservoir model was used in this study. (a): A thin and homogeneous reservoir (permeability=5·10$^{-11}$ m$^2$) located within a 3D model. (b): Three injection (I1, I2, I3) and three production (P1, P2, P3) well positions embedded in the simplified reservoir model. The dimensions of the inner reservoir are (1 km·0.6 km·1 m) and the initial reservoir temperature distribution ranges from 145°C to 175°C.**

**Table 1.** Properties of the rock (Bächler et al., 2003; Baillieux et al., 2013)

| Properties | Symbols | Units | Caprock | Outer reservoir | Inner reservoir | Bedrock |
|---|---|---|---|---|---|---|
| Porosity | ϕ | - | 0.01 | 0.1 | 1 | 0.01 |
| Permeability | $k$ | m$^2$ | 10$^{-18}$ | 5 10$^{-16}$ | 5 10$^{-11}$ | 10$^{-20}$ |
| Density | $\rho^s$ | kg m$^{-3}$ | 2600 | 2600 | 2600 | 2600 |
| Specific heat capacity | $c_p^s$ | J kg$^{-1}$ °K$^{-1}$ | 850 | 850 | 850 | 850 |
| Heat conductivity | $\lambda^s$ | W m$^{-1}$ °K$^{-1}$ | 2 | 2 | 2 | 2 |

**Table 2.** Fluid properties (L. Smith & Chapman, 1983).

| Properties | Symbols | Units | Value |
|---|---|---|---|
| *Water* | | | |
| Bulk modulus | $K_w$ | Pa | 2·10$^{10}$ |
| Density | $\rho_w$ | kg m$^{-3}$ | $\rho_w = 1000 \cdot e^{\frac{p_w}{K_w}}$ |
| Viscosity | $\mu_w$ | Pa s | 10$^{-3}$ |
| Specific heat capacity | $C_{p,w}$ | J kg$^{-1}$ K$^{-1}$ | 4000 |
| Heat conductivity | $\lambda_w$ | W m$^{-1}$ K$^{-1}$ | 0.6 |
| *Nanotracer* | | | |
| Diffusion coefficient | $D$ | m$^2$·s$^{-1}$ | 4·10$^{-12}$ |

Tracers (conservative and temperature-reporting nanotracers with different temperature thresholds) are injected only on the first day at a mass rate of 6 g·s$^{-1}$ for each tracer, whereas the injection and production flow rates of water are constant at 40 L·s$^{-1}$ for five years. The water is injected at a constant temperature of 70°C. The inner reservoir has a thickness of 1 m in the X direction and has a permeability of $5\cdot10^{-11}$ $m^2$. As shown in Figure 2 (b), the initial temperature range is 145°C to 175°C for a reservoir depth interval of 0.6 km. Three alternative injection points I1, I2 and I3 as well as production points P1, P2 and P3 have depth positions of -2.7 km, -2.8 km and -2.9 km, respectively see Figure 2 (b).

## 3 Results and Discussions

Several numerical simulations are conducted to illustrate the working mechanisms of temperature-reporting nanotracers by analyzing the response behavior from the data collected at the production well. Firstly, a case with homogeneous permeability of the inner reservoir is tested. The main purpose is to understand how the velocity field obtained from different well positions affects the breakthrough curve response of the temperature-reporting nanotracers for a given initial temperature distribution. The breakthrough concentrations of these nanotracers are analyzed by extracting the peak information (i.e., peak concentration values and peak arrival time) from their breakthrough concentration curves. Secondly, more complex features are added to the model to investigate the effect of inclined zones (with different permeabilities) embedded within the reservoir and different thermal distributions.

### 3.1 Reference Case: Homogeneous System

The temperature-reporting nanotracers we use in this example have different temperature thresholds from 145°C to 180°C with variations of 5°C. For specific and detailed investigations, the temperature threshold differences were refined to 1.25°C in part of the temperature range. It should be noted that the selected temperature threshold range of the nanotracers is valid only for our numerical model setting. In future nanotracer field tests, the temperature threshold range can be estimated from a simplified linear relationship between reservoir thickness and temperature data at or near the wellbore from the exploration and well-drilling stages. Conserved nanotracers are co-injected for comparison. Nine scenarios of injection-production position setup are simulated with the same well operating conditions, injected materials and volumetric rates.

#### 3.1.1 Interdependency among Fluid Flow, Heat Transfer, Transport and Reaction of Temperature-reporting Nanoparticle Tracers

To illustrate the temperature distribution and associated flow regimes related to the tracer test, consider two well positions: I1P1 and I1P3. The results are depicted in Figure 3 when the conservative nanotracer concentration reaches its peak concentration at the production well (80 days for I1P1 and 90 days for I1P3). The nanotracer is transported toward the production well, following the displayed fluid flow directions. The fluid (i.e., water well-mixed with nanotracers) flow direction is essentially based on the fluid velocity which is computed from Equation 2. It does not indicate its magnitude. The fluid flow direction together with the velocity field (subplots a2 and b2) reflect the streamlines of fluid flow.

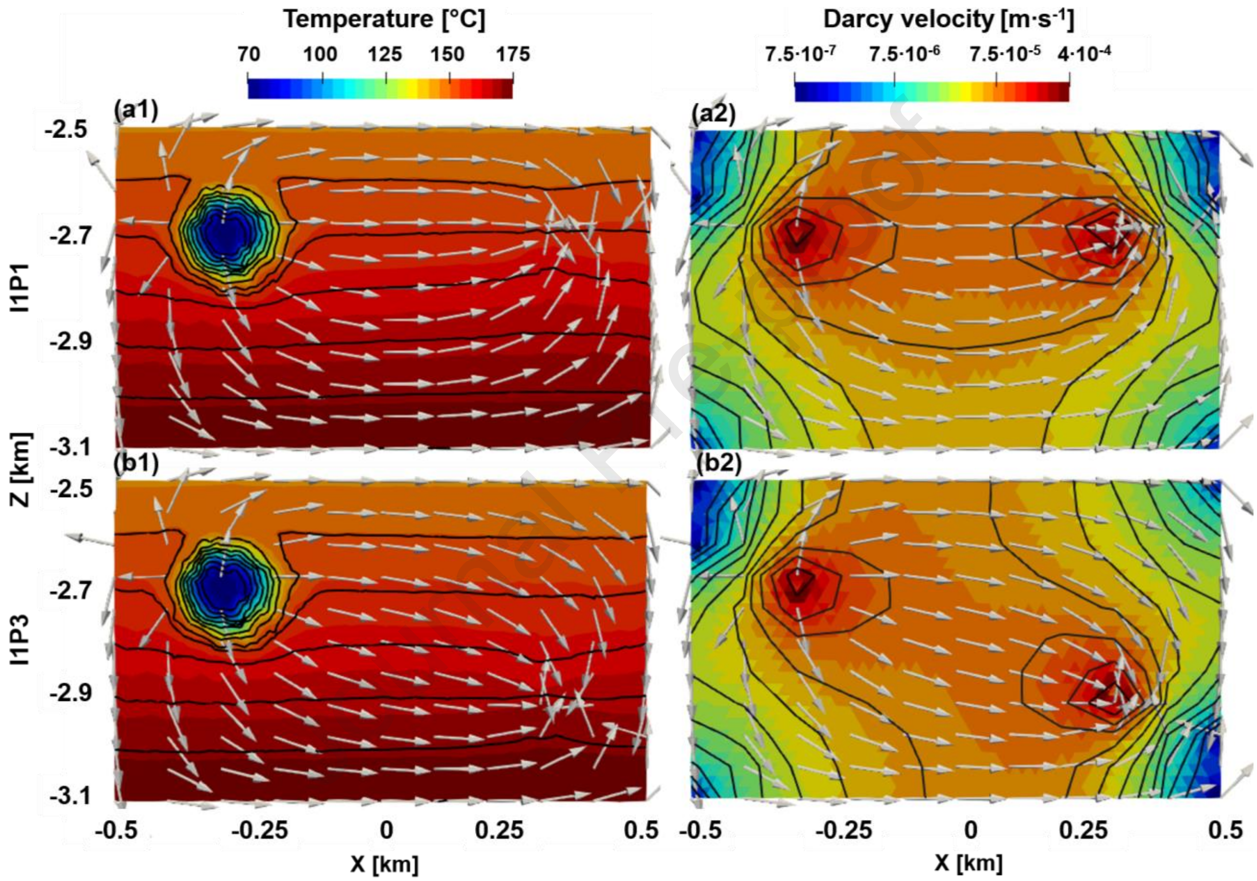


**Figure 3. Typical thermal and hydraulic states of the reservoir (depth range 2.5~3.1 km): (1) Temperature and fluid flow direction distribution and (2) velocity fields at 80 days and 90 days which correspond to concentration peaks of the conservative nanotracer collected at the production well when the injection-production points (a) I1P1 and (b) I1P3 are chosen, respectively. The black lines in (a) and (b) are the reservoir temperature contour and Darcy velocity distributions, respectively.**

The volume around the injection point cools down (Figures 3 (a1) and 3 (b1)) since the injected water has a lower temperature. The temperature field is asymmetrical due to the flow field not being aligned with the initial temperature distribution. The injected fluid sweeps the reservoir symmetrically around the main streamline region towards the production point but is affected by the reservoir boundaries. The overall magnitude of fluid velocity for both I1P1 and I1P3 (Figures

3 (a2) and 3 (b2), respectively) is similar along the main streamlines since the injection and production rates are the same.

Figure 4 illustrates the nanotracer concentration distribution for three types of nanotracers: one conservative ($C_{cons.}$) and two temperature-reporting nanotracers ($C^{prod.}_{T_{160°C}}$ and $C^{prod.}_{T_{170°C}}$) with temperature threshold 160°C and 170°C, respectively. We track only the converted temperature-reporting nanotracer concentrations ($C^{prod.}_{T_{thre.}}$) as the sum with unconverted nanotracer concentration is preserved (acting as a conservative nanotracer). Injection-production position setups are still I1P1 (Figures 4 (a) and 4 (b)) and I1P3 (Figures 4 (c) and 4 (d)). In each case, two groups of times were selected for plotting: the former are 80 days and 300 days and the latter are 90 days and 160 days, which individually correspond to the peak arrival time of conservative nanotracer and temperature-reporting nanotracer with $T_{thre.}$=170°C in the I1P1 case and the I1P3 case, respectively.

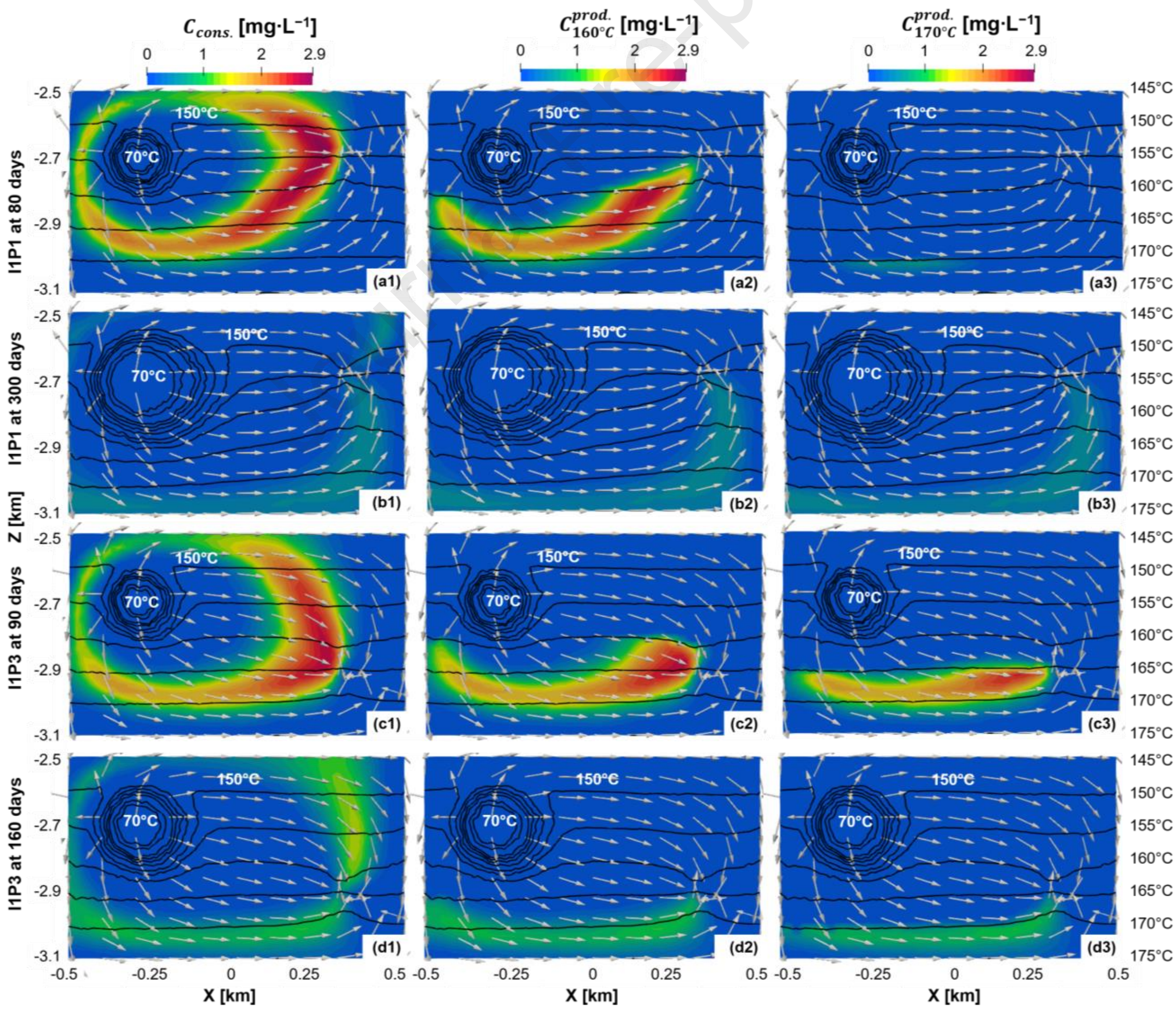

**Figure 4. Distributions of conservative nanotracer and temperature-reporting nanotracers with $T_{thre.}$=160°C, 170°C. (a, b): I1P1 setup at 80 and 300 days (peak arrival time of conservative nanotracer and nanotracer with $T_{thre.}$=170°C); (c, d): I1P3 setup at 90 days and 160 days (peak arrival time of conservative nanotracer and nanotracer with $T_{thre.}$=170°C). The black contours with their magnitudes on the right clearly show the reservoir temperature distribution.**

In the case of I1P1, conservative nanotracer flows from the injection point to the production point, covering both shallow and deep parts of the reservoir (Figures 4 (a1) and (b1)). The high-concentration part of the conservative nanotracer is best maintained along the main streamline of fluid, while the concentrations are more diffuse in the weak-current region. This is associated with the nanotracer concentrations traveling at different speeds and mixing with low fluid concentrations at neighbouring streamlines. The temperature-reporting nanotracers can react if they reach temperatures above their thresholds thus being converted. As a result, shallow and deep formations with comparatively low and high temperatures have different abilities to convert the temperature-reporting nanotracers with their corresponding temperature thresholds. From Figures 4 (a2) and 4 (a3), there are large proportions of converted temperature-reporting nanotracers with a threshold of 160°C in the lower half reservoir and only small amounts of converted temperature-reporting nanotracers with a threshold of 170°C appear in the lower quarter reservoir. Above the middle reservoir, there is zero concentration of $C_{T_{160°C}}^{prod.}$ and $C_{T_{170°C}}^{prod.}$ meaning that the corresponding nanotracers are not converted in the upper part of the reservoir. Compared to the conservative nanotracer, the two temperature-reporting nanotracers are just partly converted. Compared to the results in 80 days, the concentrations of the three nanotracers become weakened after 300 days due to continuous production. In addition, the distributions of $C_{T_{160°C}}^{prod.}$ and $C_{T_{170°C}}^{prod.}$ are similar to each other after 300 days, which reflects the slow tail production.

From case I1P1 to I1P3, the fluid flow direction has changed (see Figures 4 (a1) and (c1)). The conservative nanotracer in Figures 4 (a1) and 4 (c1), flows through a wide region and a slightly longer distance to the production point. The peak arrival time is thus longer with I1P3 than with I1P1. However, when comparing Figures 4 (b3) and 4 (d3), the peak arrival time of the nanotracer with a 170°C threshold is less with I1P3 (160 days) than with I1P1 (300 days) due to the shorter flow path to cross regions where temperatures reach above 170°C.

### 3.1.2 Well Configuration Impact on Temperature-reporting Nanotracer Breakthrough Curve

As mentioned earlier, there are a total of nine injection-production well positions. Figure 5 summarizes the nanotracer breakthrough concentrations at the production well, including both conservative nanotracer and nine converted temperature-reporting nanotracers with temperature thresholds varying from 150°C to 172.5°C.

The nanotracers are injected with the same concentration and can be directly compared. The conservative nanotracer profile is always above the other nanotracer profiles. The temperature-reporting nanotracers are converted only when their thresholds are met in certain reservoir regions.

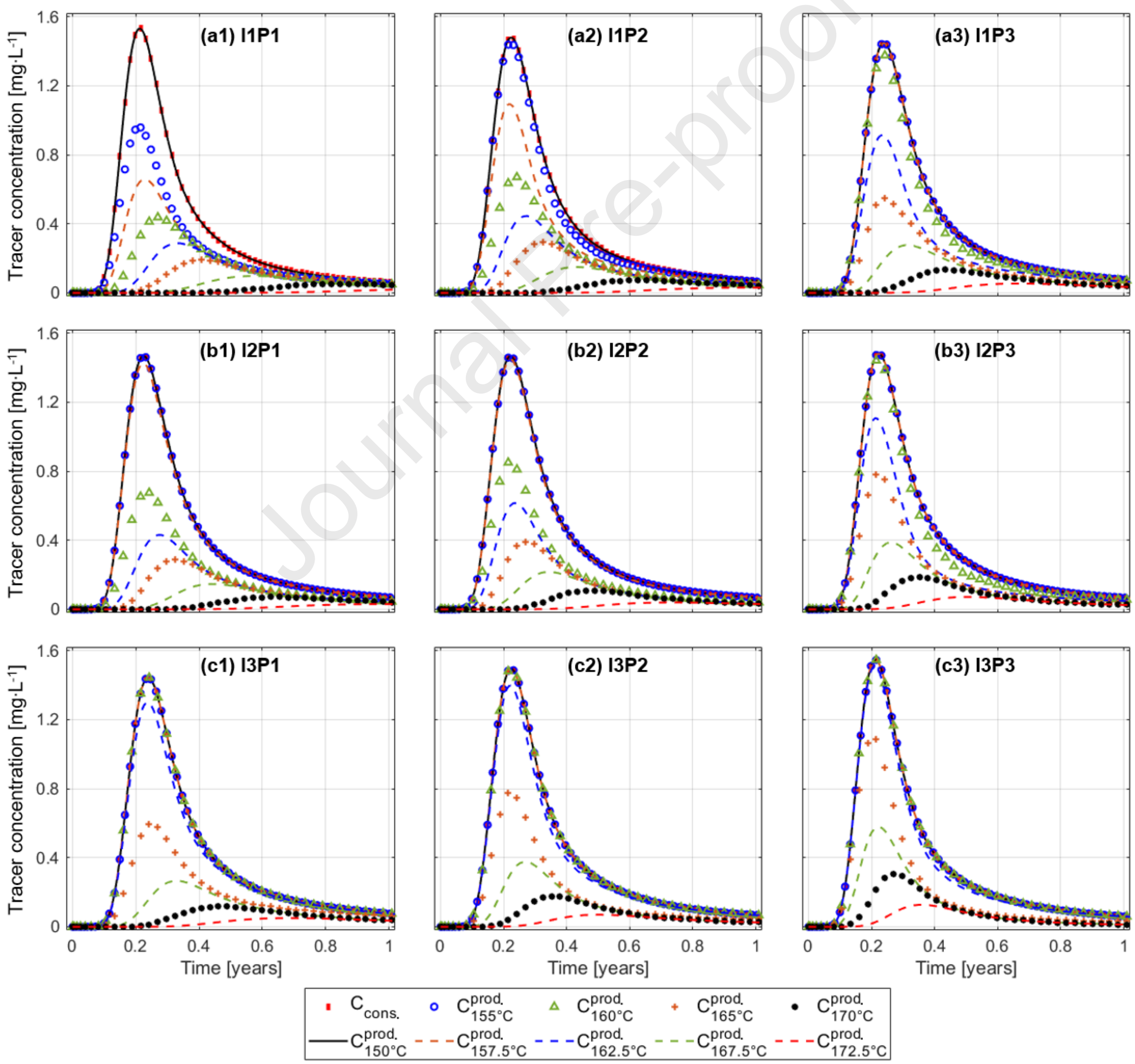


**Figure 5. Nanotracer breakthrough curves in comparison to the conservative nanotracer (blue points) with a total of nine injection-production well configurations.**

Referring to Equation 4, the sum of reactant and product concentrations equals the conservative nanotracer concentration. When a nanotracer is not fully converted, the product concentration is less than the conservative nanotracer concentration. Therefore, in all subplots of Figure 5, the curves produced by the temperature-reporting nanotracers with low-temperature thresholds, such as 150°C and 155°C, are very close to the conserved one. In addition, high peak concentration values in these nanotracer breakthrough curves normally correspond to short travel time. On the contrary, the temperature-reporting nanotracers with high-temperature thresholds such as 172.5°C are less converted and have lower peak values of concentration. They also take a longer time to reach the peak concentration than those with low-temperature thresholds such as 160°C. Nanotracers with higher thresholds have to be transported further to be converted.

The effects of injection-production positions are visible on the nanotracer breakthrough curves in Figure 5. Subplots (a1) I1P1, (b2) I2P2 to (c3) I3P3 show that the magnitude of temperature-reporting nanotracer breakthrough curves increases towards the conservative curve with deeper injection-production position. More nanotracer is converted at a greater depth with higher temperatures. The process to reach their corresponding peaks is also accelerated because the conversion happens along (or closer to) the fastest streamline. The same trends apply to the cases where well position I or P is constrained but the paired well position P or I moves towards the deep formation, referring to subplots (a1)-(b1)-(c1) in Figure 5.

The results from injection-production positions I1P3 (Figure 5 (a3)) and I3P1 (Figure 5 (c1)) differ, although the geometric settings are symmetrical. The 162.5°C nanotracer curve in subplot (c1) with I3P1 has a higher magnitude than in subplot (a3) with I1P3. This difference is due to the nanotracer starting at a high temperature in the first case, and not meeting that high temperature along all flow lines in the second case.

### 3.1.3 Analysis of Temperature-reporting Nanotracer Breakthrough Curves for Reservoir Characterization

A key factor that can be used to maximize the production of geothermal energy is the knowledge of temperature which is the main streamline of injected water experiences. Since the nanotracers follow the water, the temperature-sensitive tracer information can, ideally, reflect the temperature characteristics of the streamlines. Based on that, a new analysis method is proposed to quantify reservoir temperature information from temperature-reporting nanotracer breakthrough curves (such as Figure 5). Peak concentration values and peak arrival time are plotted versus the nanotracer temperature thresholds, see Figure 6. Temperature-reporting nanotracers with thresholds 175°C and 180°C were not converted due to the highest reservoir temperature being 175°C. Therefore, their peak concentrations in subplot (a) are zero and the peak arrival time in subplot (b) does not exist. Here we need to mention that it is important to use a broad range of nanotracer temperature thresholds to cover the reservoir temperatures since the exact temperature distribution is unknown in realistic field tests.

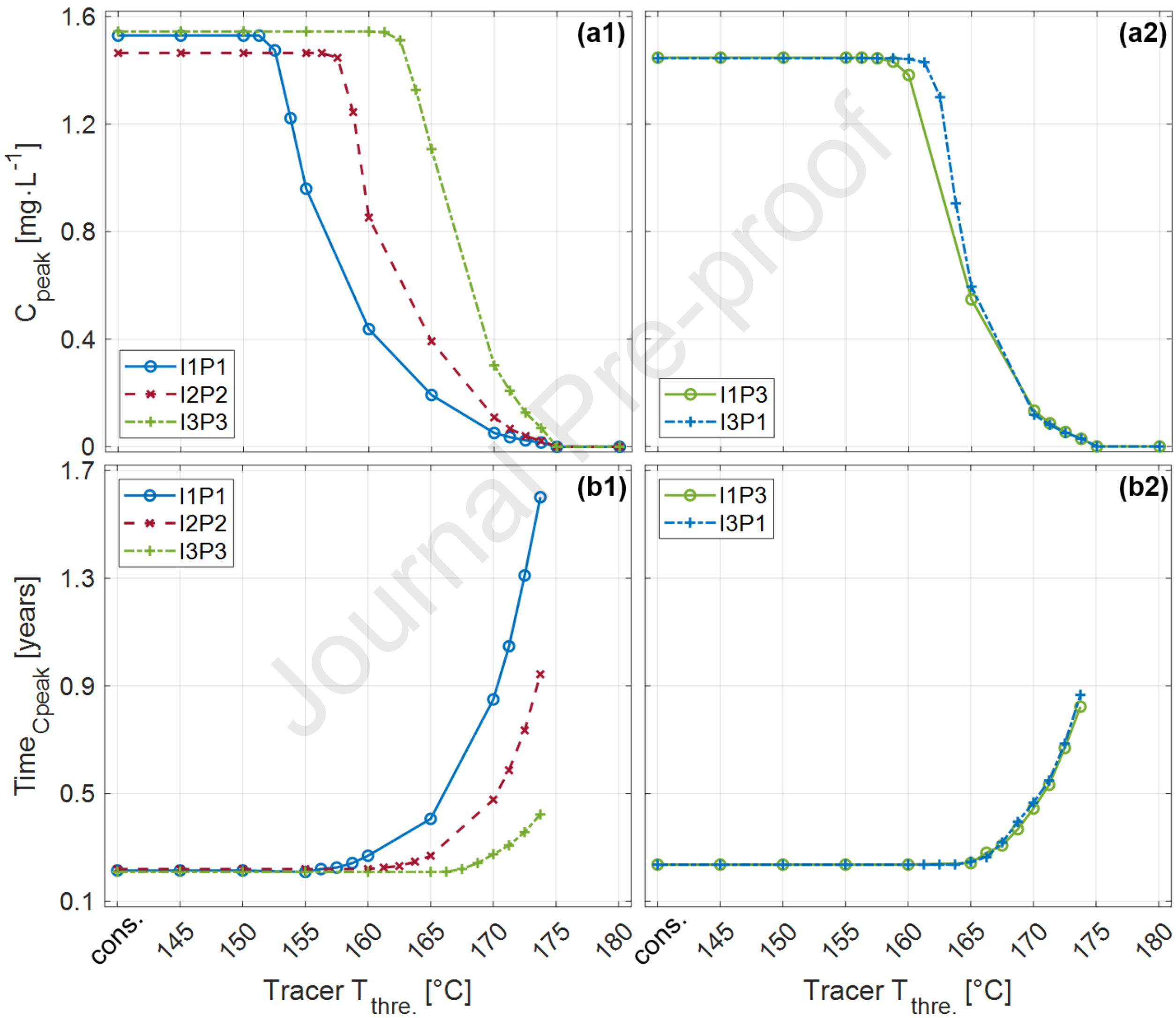


**Figure 6. Comparison of peak concentration (a) and peak arrival times (b) of the individual nanotracer types from the nanotracer breakthrough curves for different well configurations. Thresholds from 145°C to 180°C and conservative nanotracers are shown.**

The curves of both peak concentration value and peak arrival time versus threshold temperature have flat sections at low-temperature thresholds, which correspond with the conservative nanotracer, indicating full conversion. The temperature encountered on the flow paths between the wells must therefore be above these thresholds.

When the peak concentration curves deviate from the flat sections, for a nanotracer with a sufficiently high threshold temperature, some of that nanotracer has traveled along a flow path with a temperature below the threshold where it was not converted. In other words, the threshold temperature at the transition from fully converted nanotracers to less converted nanotracers indicates that there are flow paths not exceeding this indicated temperature. This provides an upper limit of the lowest temperature in the flow region. Similarly, when the threshold temperature of the nanotracers becomes sufficiently high, they are not converted (zero peak concentration) indicating no flow paths reach that high temperature. Thus, the threshold temperature where the nanotracers firstly stop being converted is an indication and approximation of the highest temperature in the flow region. As the sum concentration of nanotracer reactant and product acts like a conservative nanotracer, this holds regardless of reservoir properties (this could change if the nanotracer interacted chemically different within the reservoir).

As indicated, there is an important precaution regarding the history-dependent behavior of the nanotracers. If they have passed through a region above the threshold temperature, they are activated regardless of what happens later. Consider the difference between injection from a deep towards a shallow producer, with injection from a shallow position towards a deep position. (i) In the former case the high temperature is at the injector and the different nanotracers are exposed to high temperature from the start. They might not see much higher temperatures and although there are lower temperatures downstream, they are already activated, yielding a narrow range for the deviation thresholds. Such a case mainly provides reliable information about the highest temperature. (ii) In the latter case the nanotracers are exposed to a low temperature at the injector and take multiple directions having different temperatures towards the producer. The initial high-temperature fluid at the producer is produced before the nanotracers encounter it, meaning the maximum interpreted temperature may be less than the initial temperature at the producer. Some flow paths can however go deeper to reach even higher temperatures.

In the following, the nanotracer temperature threshold at the turning point of each nanotracer curve is discussed and compared to the temperature along the injection-production positions. Consider first the injector-producer pairs positioned at the same depth. In Figure 2 (b), the initial temperatures of I1P1, I2P2 and I3P3 are 155°C, 160°C and 165°C, separately. In Figure 6 (a1) the peak concentration values deviate at 151.25°C, 156.25°C and 161.25°C, respectively. This means not all the injected nanotracer was converted by the initial temperature surrounding the injector. Keep in mind that the nanotracer mixture (and then water) is injected at 70°C and thus the nanotracer needs some residence time to reach a higher temperature. As seen in Figure 3 (a1) there is a low-temperature region near the injector, while the temperature distribution in the rest of the reservoir is less affected. Some nanotracers, particularly the end of the slug, can follow paths that do not reach the high initial temperatures. Concerning the peak arrival time in Figure 6, we observe a deviation from the horizontal section at 155°C, 160°C and 166°C, which corresponds more closely with the initial temperatures at the injectors and producers. In Figure 6 (a1), nanotracer peak concentrations become zero when the temperature threshold approaches 175°C. This means the maximum temperature of the overall reservoir is below 175°C (as confirmed in Figure 4). While this high temperature was detected in all three cases, the lowest temperature of the reservoir of 145°C (see Figure 4) was not detected by any. Flow lines were passing through temperatures below 150°C for the case I1P1 (Figure 4), thus 145°C might have been expected to be the highest stable point. Likely, each flow line contained a region (close to the well) with a higher temperature that activated the nanotracers, as suggested before. From the above analysis, we conclude that it is generally difficult to estimate the lowest temperatures in the reservoir. However, when the wells, especially the injector, are placed shallower, the threshold temperature where the peak concentrations start to decrease, becomes better, but not reliable, estimates of the minimum temperature.

The results of inclined wellbore positions I1P3 and I3P1 are shown in Figures 6 (a2) and (b2). As seen in Figure 4 for I1P3, flow lines pass through both regions below 150°C and above 170°C and the same is true for I3P1 by symmetry. For both cases, the concentration curves flatten precisely at 175°C, as for the three previous cases, indicating the maximum temperature of 175°C. The peak concentrations of I1P3 and I3P1 cases deviate at 157.5°C and 160°C, respectively, close to the initial temperature of 160°C centrally between the two wells (Figure 2). This reflects that nanotracer needs to flow through regions with this temperature whether it flows from the deep or shallow configuration. Especially in Figure 4, we see that for I1P3 all flow lines cross a temperature of 160°C at the indicated time. The deviation threshold temperature is higher for I3P1, related to the nanotracer encountering higher temperatures from the start. In Figure 6 (b2), the peak arrival time deviates for both I1P3 and I3P1 at a temperature threshold of 165°C. This is closer to the deeper wellbore's initial temperature.

It is noticeable that the peak concentrations deviate at lower temperature thresholds than the arrival time. As seen in Figures 6 (a) and 6 (b), the peak concentrations reduce while their arrival time stays the same. This is related to where the nanotracers are flowing. The peak of the conservative nanotracer represents the flow from the fastest flow lines between the wells. When the nanotracer is converted along the same lines, we also see the arrival of that nanotracer with the same peak, however, when the nanotracer needs to take a longer path to be converted, the arrival time is increased. Several of the colder streamlines at the top of the reservoir may supply an unconverted nanotracer, yielding less production and a lower peak concentration of the converted nanotracer. But as long as the main flow line between the wells has sufficient temperature the arrival time is similar to the conservative nanotracer. Similarly, we can suggest that the higher peak arrival time represents the time needed for nanotracers with the indicated thresholds to pass through flow lines with those temperatures. In Figure 6 (b1) the arrival time of a nanotracer with a given threshold decreases when the horizontally positioned well pair is deeper, because the main flow line has a higher temperature and activates more nanotracers there, and because the nearby flow lines also have a higher temperature. At shallow locations, the nanotracer needs to follow a long flow path to be activated. Considering the inclined positioned wells (Figure 6 (b2)), the arrival time profiles are almost identical. They deviate from the flat section when the threshold temperature exceeds the highest temperature of 165°C along the main flow line. Only flowlines deeper than the well pair reach higher temperatures. With the flow pattern being symmetrical and most of the temperature distribution remaining as the initial, the nanotracers are activated in the same flow lines for the two cases and get the same arrival time.

To summarize the main points, temperature-reporting nanotracer breakthrough curves can be interpreted as follows:

- The nanotracer peak concentrations as a function of threshold temperature:
    - Deviate from full conversion at a threshold temperature which is an upper limit of the lowest temperature encountered along all the flow lines. This is not a reliable estimate of the minimum temperature.

  - First reaches a zero value at a threshold temperature which is a precise estimate of the maximum temperature in the flow region. The estimate is improved by using multiple tracers with small differences in the temperature thresholds.
- The nanotracer arrival time as a function of threshold temperature:
  - Deviates from the arrival time of the conservative nanotracer at a threshold temperature equal to the highest temperature along the fastest/main flow line between the wells. This deviation temperature is usually higher than that from the nanotracer peak concentration curve.
  - Higher arrival time on the curve indicates the time needed to flow along lines reaching the corresponding threshold temperatures.

In the following sections, we utilize the presented analysis method on more complicated reservoir conditions, including **Section 3.2** different thermal distributions (varied temperature ranges at certain depths and regional thermal anomalies) within the geothermal reservoir and **Section 3.3** inclined zones embedded within the reservoir. The purpose of these investigations is to determine the impact of these thermal and geological uncertainties on the analysis of performance evaluation of temperature-reporting nanotracers in geothermal reservoirs. Schematic illustrations of varied temperature ranges, regional thermal anomalies and inclined zones are shown in Figure 7 (a-c), respectively.

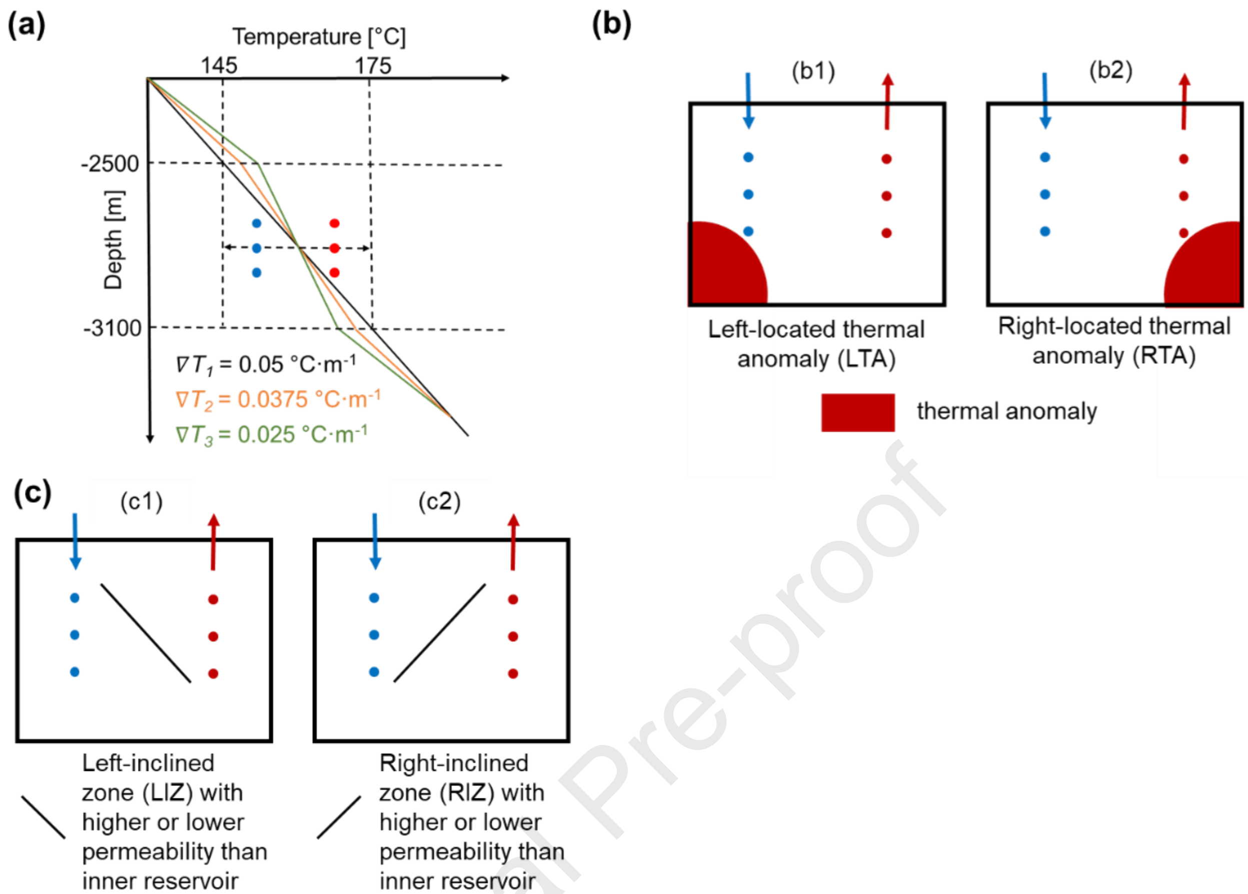


**Figure 7. Schematic representation of geological heterogeneities and temperature anomalies in a reservoir (a): Different initial temperature ranges with gradients $\nabla T$ = 0.05°C·m$^{-1}$, 0.0375°C·m$^{-1}$ and 0.025°C·m$^{-1}$ along the inner reservoir depth from -2500 m to -3100 m; (b) Lower-left or lower-right located high-temperature regions within the inner reservoir; (c): Left-inclined (LIZ) or right-inclined zones (RIZ) with higher, same, or lower permeabilities compared to the inner reservoir. Note that the inclined zone with dimensions (1000 m·600 m·1 m) is a plane perpendicular to the thin reservoir.**

## 3.2 Impact of Different Thermal Distributions in the Fractured Geothermal Reservoir

Temperature distributions and heat flux densities in the subsurface can vary greatly depending on location. Values above average are referred to as positive anomalies. Conversely, a negative anomaly indicates a decrease in temperature or heat flux relative to the surrounding mean. Thermal anomaly in subsurface formations is a common geological phenomenon that can be caused by variations of thermal conductivities around structures such as salt domes, geological and tectonic activity, geochemical reactions, or hydrothermal activities in faults and fractures (Cherubini et al., 2013; Emry et al., 2020; Yan et al., 2023). Subsurface formations with positive thermal anomalies are targeted as areas of geothermal development for heat and electricity production (Moeck, 2014). In the following, we investigate two scenarios impacted by different local temperature gradients or a positive regional thermal anomaly and whether they are detectable by the nanotracer analysis.

### 3.2.1 Different Temperature Ranges

We consider three different initial temperature gradients as shown in Figure 7 (a) where the middle of the reservoir is constrained to 160°C. Here, cases 1, 2 and 3 respectively correspond to temperature gradients of 0.05°C·m$^{-1}$, 0.0375°C·m$^{-1}$and 0.025°C·m$^{-1}$, with initial reservoir temperature ranges of 145°C~175°C, 148.25°C~170.75°C and 152.5°C~167.5°C. Note that only the initial reservoir temperature range is varied in the numerical model; the remaining parameters are the same as in the reference case. Case 1 is essentially the reference case studied in **Section 3.1**.

The resulting concentration peak and arrival time trends from the nanotracer breakthrough curves are shown in Figures 8 (a) and 8 (b) for injection-production position setups I1P1 and I1P3. There is an obvious distinction among the curves of the three cases with different initial temperature gradients. In Figure 8 (c) the curve deviation temperatures are compared with initial well temperatures (red markers) and initial reservoir temperature range (grey bars) for additional well setups. Each curve in Figures 8 (a1) and 8 (a2) flattens at zero concentration at a high temperature. As discussed, this point indicates the maximum temperature, which is confirmed to be accurate by the comparison (top of the grey bar and top green point) in Figures 8 (c1) and 8(c2). The lower temperature deviation on the concentration curve, however, does not reliably estimate the minimum reservoir temperature and is in some cases above the lowest initial well temperature and, and some cases below. The deviation temperature of the arrival time curve (blue marker) has been noted to reflect the maximum temperature along the streamline between the wells. As the reservoir is homogenous, this flow line goes directly between the wells and the maximum temperature of this flow line is likely to be approximately the highest initial well temperature. This comparison (blue point and highest red point in Figure 8 (c) is very accurate (0 to 2°C difference) for all 10 cases. We have thus demonstrated accurate prediction of the highest reservoir temperature and main streamline temperature.

When the initial temperature range (i.e. local gradient) increases the estimated max temperature increases accordingly. For the horizontally positioned wells, a higher gradient (thus lower min temperature) is reflected in a lower min temperature estimate for I1P1, but when the wells are positioned deeper (I2P2 or I3P3), there is little to no difference with the gradient. The flow lines then start at hotter temperatures (slightly below the initial well temperature) and activate according to higher temperatures than found at the top of the reservoir. Changing the gradient for

572 I1P3 also has little effect on the lower limit temperature estimate, as the flow lines all pass 160°C
573 in the center.

574

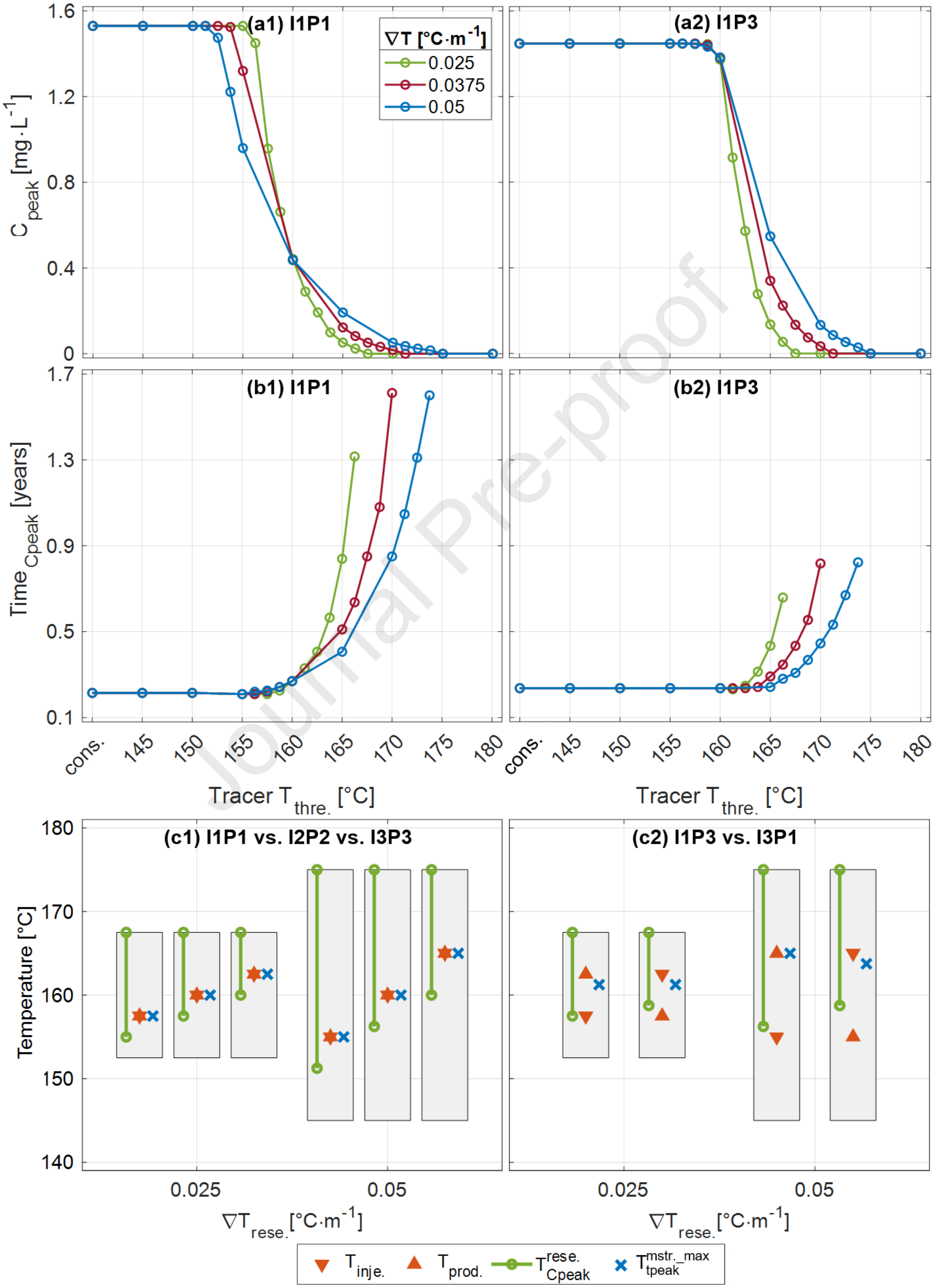

**Figure 8. Comparison of nanotracer performance for peak concentration (a), peak time (b) and estimated reservoir temperature data (c) for initial temperature gradients $\nabla T$ = 0.025 or 0.05°C·m$^{-1}$. Well configurations are indicated. $T_{inje.}$ and $T_{prod.}$ are initial temperatures at injection and production positions, while grey bars indicate the reservoir's initial temperature range. $T_{C_{peak}}^{rese.}$ show estimated reservoir temperatures based on peak concentration curve deviation. $T_{t_{peak}}^{mstr.\_max}$ is the temperature where the arrival time curve deviates (estimating the highest temperature on the main streamline between the wells).**

The temperatures between the concentration turning points indicate a possible reservoir temperature range. For a given well positioning the jump of each curve in Figure 8 (a1) or (a2) will become sharp when the temperature gradient decreases. Regardless of the initial temperature gradients of the reservoir, subplot (c1) shows that the low reservoir temperature obtained is dependent on the tested positions, the maximum temperature can always be detected, and shallow tested locations such as horizontal I1P1 exhibit more effectiveness in measuring reservoir temperature intervals. Looking at the inclined cases I1P3 and I3P1 in subplot (c2), the estimation performance for reservoir temperature ranges looks pretty generic.

### 3.2.2 Regional Thermal Anomalies

High-temperature regions are artificially added to the reservoir in the lower-left or lower-right positions to mimic regional positive thermal anomalies of up to 200°C from deep radiant heat sources, see Figure 7 (b). Note that only the high-temperature regions are added to the numerical model, the remaining parameters are the same as in the reference case. The temperature thresholds of the nanotracers have extended from 145°C~180°C to 145°C~205°C with variations of 5°C. For specific and detailed investigation, the temperature threshold difference is refined to 2.5°C in part of temperature ranges. We compare tracer results in Figure 9 (a, b) for a homogeneous case without thermal anomaly (HOM), a case with left thermal anomaly (LTA), and a case with right thermal anomaly (RTA).

The high-temperature region enhances the conversion of temperature-reporting nanotracers with high thresholds in the deep reservoir, see subplots (a1) and (a2). The cases with LTA and RTA produce nearly the same results for I1P1 in subplot (a1), probably because the streamlines are symmetric in the left-right direction and the cooled-down region due to injection has not affected the high-temperature distribution in the deep reservoir during the given period. Nevertheless, when the injection-production position is changed to the inclined I1P3, the difference between LTA and RTA is clearly distinguishable in subplot (a2) where the case with RTA results in higher peak concentration values than with LTA. The streamlines from I1 to P3 flow through the high-temperature region on the right side (RTA) close to P3 rather than the left

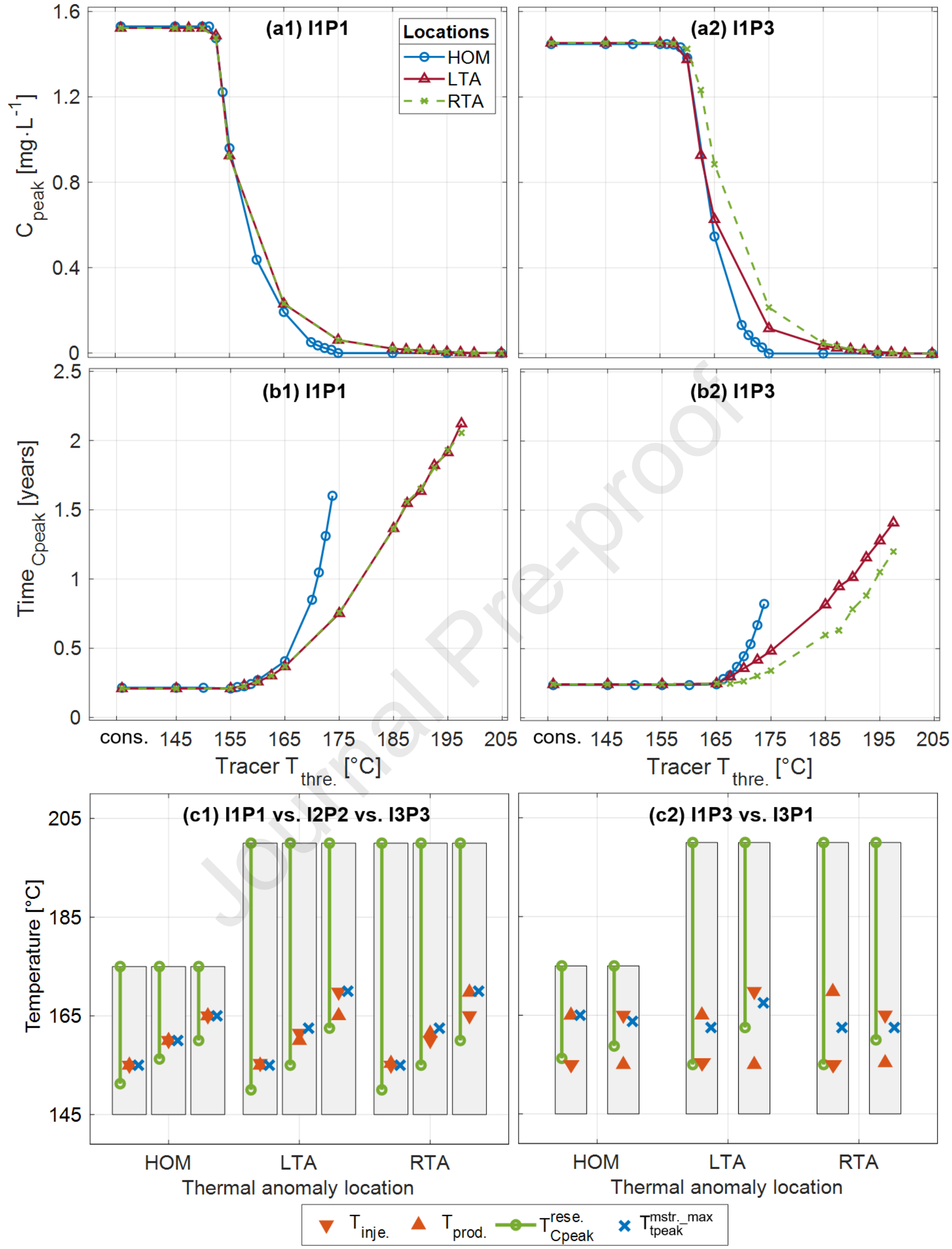


**Figure 9. Comparison of nanotracer performance for peak concentration (a), peak time (b) and estimated reservoir temperature data (c) in models with no (HOM), left-located (LTA) or right-located (RTA)different thermal anomalies. Well configurations are indicated. $T_{inje.}$ and $T_{prod.}$ are initial temperatures at injection and production positions, while grey bars indicate the reservoir's initial temperature range. $T_{C_{peak}}^{rese.}$ show estimated reservoir temperatures based on peak concentration curve deviation. $T_{t_{peak}}^{mstr.\_max.}$ is the temperature where the arrival time curve deviates (estimating the highest temperature on the main streamline between the wells).**

one (LTA) which is not close to either well. For I3P1 the resulting behavior between RTA and LTA is opposite.

In subplot (b), the trends of the curve's relative position are similar to those plotted based on peak concentration values in subplot (a). It should be mentioned that a high-temperature region in the reservoir could behave similarly to the one with large temperature gradients when comparing Figure 9 (a, b) to Figure 8 (a, b). Specifically, the low-temperature gradient case (0.025°C·m$^{-1}$) in Figure 8 (a, b) always gives a narrow threshold temperature range which is also seen in the behavior of the HOM case without high temperature anomaly in Figure 9 (a, b). Moreover, based on the results presented in Figure 9 (a2, b2), we are able to distinguish the differences caused by the existence of thermal anomalies as well as the locations of thermal anomalies in the reservoir, when the injection-production well configuration is inclined.

A performance evaluation of the nanotracers in the reservoir with thermal anomalies is given according to the breakthrough curve peak analysis (Figure 9 (a, b)) for selected cases. The maximum temperature within the reservoir is estimated accurately, which means the thermal anomaly is detected. Although a shallow injection-production position can help to more accurately estimate the reservoir temperature range as seen in Figure 9 (c1), this effect is reduced when a thermal anomaly with high temperature is located in the deep reservoir, including both RTA and LTA. This observation is also valid for inclined well positions, see subplot (c2), when comparing the case HOM with the cases LTA and RTA. The temperature where the peak arrival time curve deviates indicates the highest temperature along the main streamlines between the wells and in most cases corresponds well with their highest initial temperature.

### 3.3 Impact of Geological Heterogeneities Resulting from Inclined Zones

Reservoirs are usually highly heterogeneous and some distinguishing features are large spatial differences in reservoir permeability. In some cases, low permeable zones are encountered, such as faults developed by tectonic movement; high permeability layers exist in other cases, such as thief zones due to possible clay erosion or sand production after a long period of water injection (C. Lu et al., 2021). Tracer testing can identify the properties of fractures or inclined zones, dependent on the shapes of tracer breakthrough curves (J. Li et al., 2016; L. Li et al., 2017). Those studies mainly focused on the conservative tracer, while here we will explore how such geological features affect the performance of temperature-reporting nanotracers in fractured geothermal reservoirs.

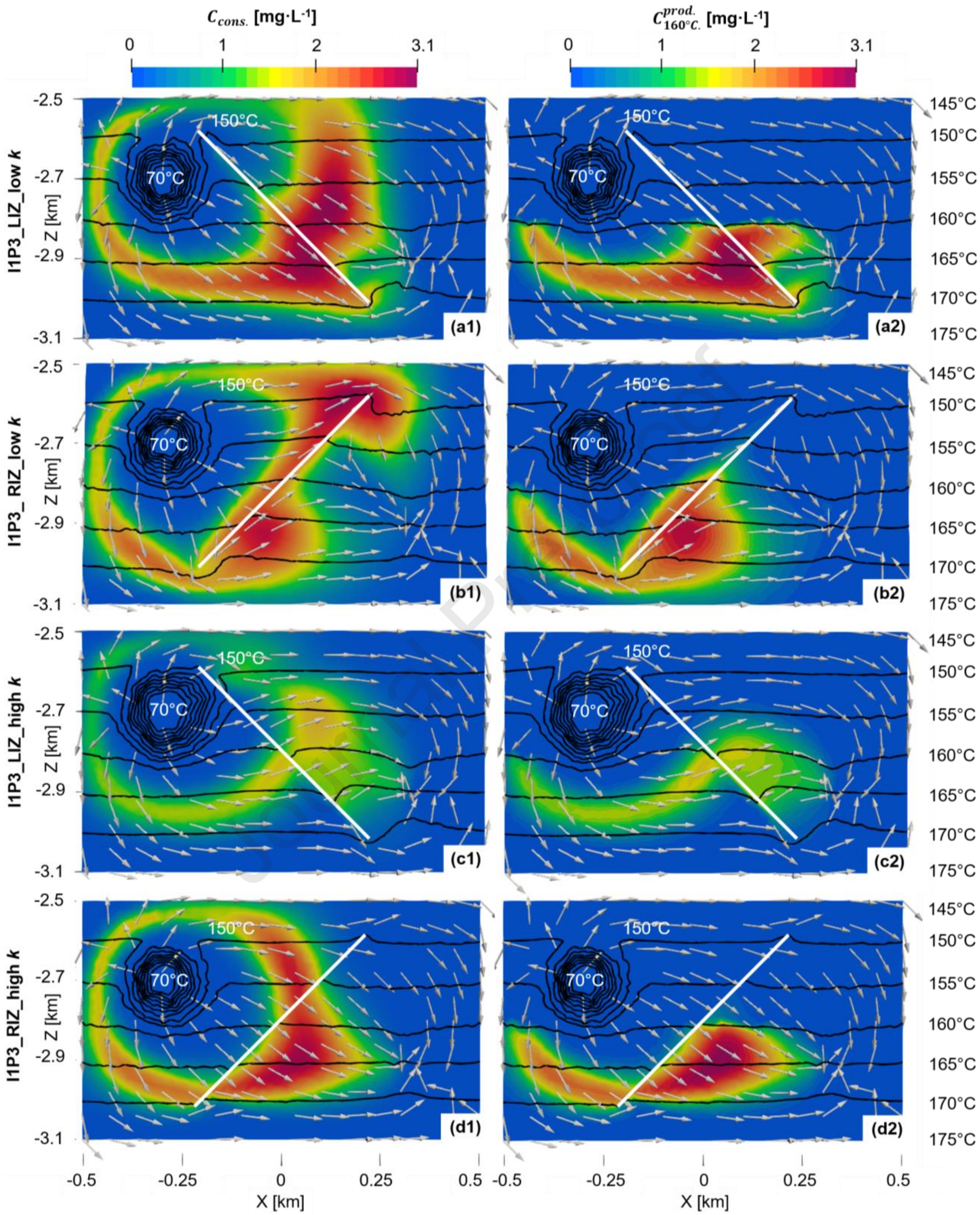


**Figure 10. Tracer concentration distributions after 70 days for a geological heterogeneous model, i.e. an inclined zone (white line) and configuration I1P3. The difference between a conservative tracer (left column) and a temperature-reporting nanotracer ($T_{thre.}$=160°C, right column) is clearly demonstrated in dependence of the hydraulic setting. Subplot a/b: low-permeable left-/ right-inclined zone (i.e., $5 \cdot 10^{-16}$ $m^2$); Subplots c and d:**

**high-permeable left and right-inclined zone (i.e., $5\cdot10^{-10}$ m$^2$). Note that the permeability of the inner reservoir is $5\cdot10^{-11}$ m$^2$. The black contours with their magnitudes on the right show the reservoir temperature.**

Figure 7 (c) illustrates a thin inclined zone centrally placed between the wells. The effects of left-inclined and right-inclined zones are studied with permeabilities higher (i.e., $5\cdot10^{-10}$ m$^2$) or much lower (i.e., $5\cdot10^{-16}$ m$^2$) than the inner reservoir permeability (i.e., $5\cdot10^{-11}$ m$^2$). Note that only the inclined zones with different directions and permeabilities are added to the numerical model, the remaining parameters are the same as in the reference case. As illustrated in Figure 10, concentration distributions of a conservative tracer and a temperature-reporting nanotracer with a 160°C threshold are shown with injection-production setup I1P3 at 70 days (when tracers flow through the inclined zone). The results with a low-permeable inclined zone are given in Figure 10 (a, b), and those with a high-permeable inclined zone are shown in Figure 10 (c, d). As expected, the temperature-reporting nanotracer with a 160°C threshold mainly exists in the lower part of the reservoir where it is converted whereas the conservative tracer has a large area of distribution in the reservoir.

In the cases with a low-permeable inclined zone, the inclined zone behaves as a tight barrier for tracer transport and tracer concentrations are separated. In subplot (a2) there is a region of high-concentration converted tracer above the inclined zone. Temperature-reporting tracer has been transported around the upper region of the reservoir (above the inclined zone) and converted after passing the 160°C isotherm.

In the cases with a high-permeable inclined zone in Figure 10 (c, d), we notice in subplots (c1) and (c2) that the fluid flow is attracted up towards the high permeability zone giving a more horizontal flow in the reservoir. This flow diversion is less clearly seen in subplots (d1) and (d2) since the direction of I1P3 is perpendicular to the right-inclined zone. The concentration of conservative tracer is less in subplot (c1) than in subplot (d1). The conservative tracer meets the high-permeable zone earlier in subplot (c1) and more tracer transports to the high-permeable zone where the tracer can be accumulated, compared to subplot (d1). Moreover, since the fluid flow is attracted towards a horizontal direction in the upper part of the reservoir in subplot (c2), less temperature-reporting nanotracer transports downward being converted than in subplot (d2).

A comparison of the tracer peak concentration and peak arrival times is shown in Figure 11 for two configurations: I1P1 and I1P3. As seen in Figures 11 (a1) and (b1) the results for I1P1 are very similar when comparing whether the inclined zone is left or right-oriented for a given permeability, due to symmetry. For I1P3, left- or right-inclined orientations do not give symmetrical flow and thus the orientation of the inclined zone impacts the tracer profiles, see curves in Figures 11 (a2) and (b2). Referring to Figure 10 (c1), a high-permeable inclined zone can divert flow towards it and attract tracers to flow in its plane from the reservoir, resulting in low peak concentration values. The separation effect on the tracer transport due to the low-permeable inclined zone can decrease the peak concentration collected in the production point, referring to Figure 10 (b1). In Figure 11 (a1) the (red) curves of peak concentrations for low-permeable inclined zone take an abrupt turn at 155°C. This is the result of a low permeability zone forcing tracers to flow in the lower part of the reservoir, as we can see in Figure 10 (a2). In the

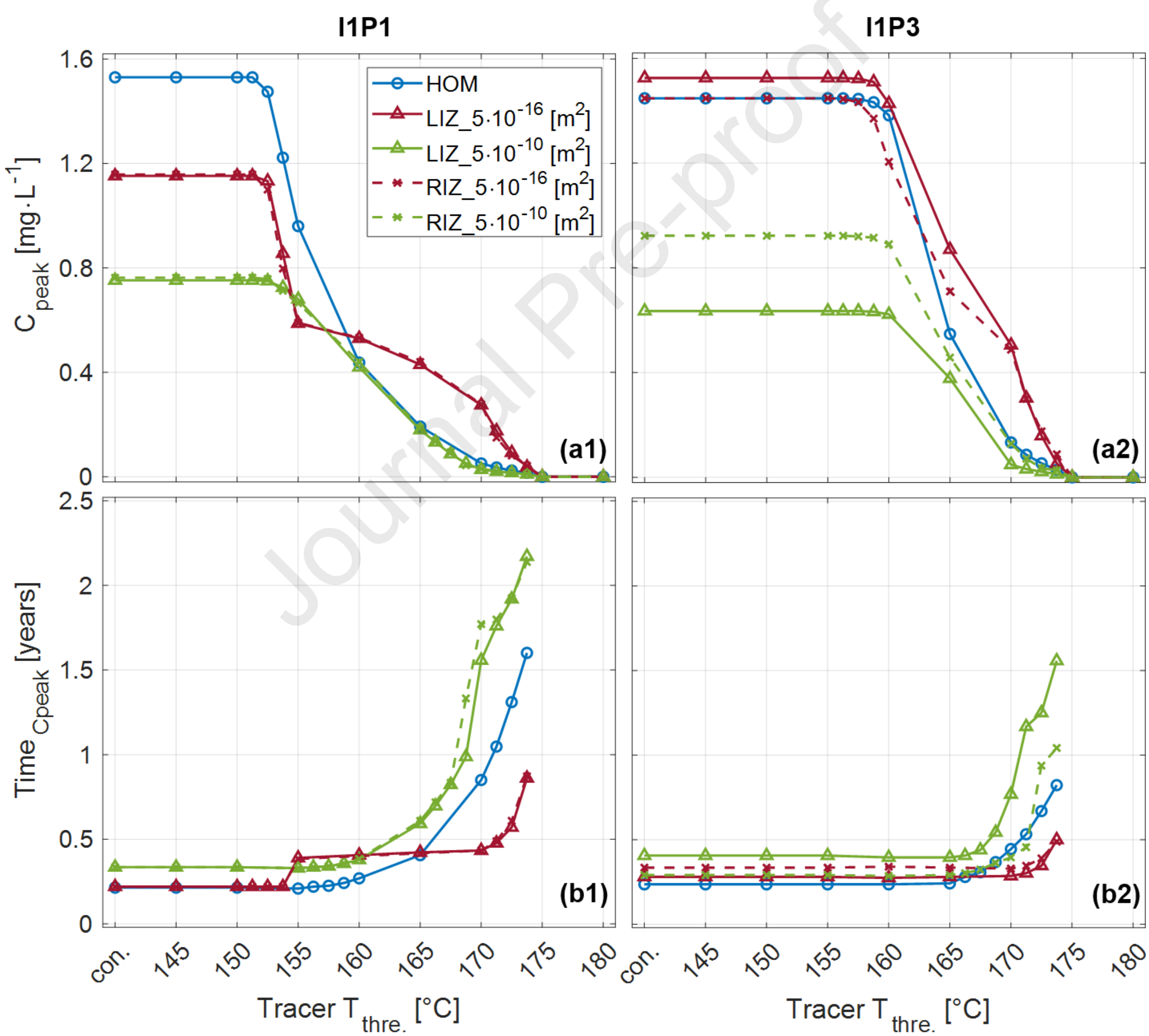


**Figure 11. Comparison of tracer performance for peak concentration (a) and peak arrival time (b) in homogeneous (HOM) and geological heterogeneous models (LIZ or RIZ) with well configurations of (1) I1P1 and (2) I1I3. The permeability in the left- or right-inclined zone (LIZ or RIZ) is $5{\cdot}10^{-16}$ m$^2$ or $5{\cdot}10^{-10}$ m$^2$ while the reservoir permeability is $5{\cdot}10^{-11}$ m$^2$.**

I1P1 setup, the fastest streamline will be at the top and stay above 155°C (the initial well temperatures) and not deliver converted tracers with higher thresholds. Streamlines that take the opposite side of the barrier will all have reached 170°C which explains the jump in arrival times at 150°C to a higher stable value until 170°C, where only the outermost streamlines can convert the tracers. As the threshold increases gradually less tracer is converted but following a different trend than at first since the tracer is primarily converted at the bottom of the reservoir. Note that the discontinuity in arrival time and the trend of peak concentration happen at the same temperature and are clear indicators of two separate flow line groups. While there were two separate streamlines groups also for I1P3, they arrived at similar times, while the reactive tracer mainly converted in the lower one.

Figure 11 (2) gives the results when the injection-production position changes to I1P3 which is exactly the setup shown in Figure 10. When the inclined zone is low permeable and the orientation is similar to the injection-production direction, the tracer transport will be efficient and give rise to high peak concentration values of tracer concentration in the production point. That is why it is seen in Figure 11 (a2) that the dashed red line (right-inclined) has a lower magnitude than the solid red line (left-inclined). On the other hand, the green dashed line in Figure 11 (a2) has higher values than the green solid one since the attraction of the high permeable zone plays a more significant role in reducing the tracer concentration in the latter case (solid line, left-inclined), which has been discussed in the above for comparisons between Figure 10 (c) and (d). Therefore, inclined injection-production position I1P3 is useful for the test to differentiate the right- or left-inclined zones. In addition, it is noticeable in Figure 11 (a) that the curve trends within the high tracer threshold range of 165°C~175°C are similar: top (low permeable zone), middle (homogeneous) and bottom (high permeable zone).

Regarding reservoir temperature estimation using the deviation points of the peak concentration and peak arrival time curves in Figure 11, we find that the maximum temperature is correctly estimated to be 175°C in all cases. For a given well setup a fairly consistent minimum temperature is estimated as 152°C~153°C for I1P1 and 157°C~158°C for I1P3 although the actual minimum for all cases is 145°C. The highest temperature of the coldest streamline is determined by how deep they go, i.e. the depth of the wells, as explained earlier. The deviation threshold temperature of the arrival time curve shows different trends compared to the homogeneous case. When there is a barrier, the flow is concentrated and it can be diverted from or towards the well, but also from or towards the higher temperatures. In the example of I1P3 with a low permeability RIZ (see Figure 10 (b2)) the flow is diverted straight down (increasing the arrival time of the conservative tracer), exceeding 170°C and then straight towards the producer. The deviation of the arrival time (red curve in Figure 11 (b2)) correctly indicates that temperatures have exceeded 170°C on the main streamlines.

## 4 Conclusions

Temperature-reporting nanoparticle tracers, which quickly, fully and irreversibly convert when the environmental temperature reaches its threshold value, were studied to characterize the temperature information of geothermal reservoirs. We developed a numerical modeling approach to illustrate their working mechanisms in a thin 3D reservoir. A mixture of tracers with different temperature thresholds was injected. First, a homogeneous and fractured geothermal reservoir was studied with nine injection-production well configurations. Furthermore, adding heterogeneities such as thermal anomalies and inclined zones were investigated. The following conclusions can be made:

- Reservoir temperature can be changed due to cold water injection and fluid intrusion from different depths. The injected temperature-reporting nanotracers travel along all streamlines but are converted on a streamline only if they reach the temperature threshold of that specific tracer. This happens if the streamline goes sufficiently deep or sufficiently close to a thermal anomaly.
- Injection-production positions and inclined high- or low-permeable zones embedded within the reservoir influence the streamlines, thus impacting the collected tracer breakthrough data. Deeper well positions steer all the streamlines through higher temperatures, while the mentioned zones can spread or deviate streamlines towards or away from the high temperatures.
- The peak concentration of a given temperature-reporting nanotracer is determined by the proportion of the swept reservoir area above its temperature threshold. The changes in tracer peak arrival time result from alterations in the flow paths of its main streamlines. A long flow path generally corresponds to a long peak arrival time of the tracer.
- A new analysis method was proposed, based on plotting the peak concentration and arrival time of each tracer against their temperature threshold.

- At sufficiently low temperatures, all tracers are fully converted, giving the same peak concentration as the conservative tracer. The temperature where the tracers start to yield lower peak concentrations is an upper limit of the minimum reservoir temperature.
- At sufficiently high temperatures, no tracer is converted, giving zero peak concentration for higher temperatures. The temperature threshold where the peak concentrations first become zero is identical to the maximum reservoir temperature.
- The arrival time of the tracer peak is the same as the conservative tracer as long as it is converted on the main (fastest) flowline between the wells. The threshold temperature when the time starts to increase indicates the highest temperature on the main flowline.

- The range in temperature thresholds between the deviations on the peak concentration curve reflects only a part of the reservoir temperature range, but the highest temperature deviation corresponds to the highest reservoir temperature, while the lowest deviation temperature can be near or far away from the lowest reservoir temperature. Changing the reservoir temperature conditions (with other conditions the same), consistently changes the max temperature (actual and estimated) but may not necessarily impact the lower threshold deviation temperature. While a reduced temperature range may be expected to reduce the difference between the thresholds (a sharper peak concentration curve), a sharp curve does not directly imply a narrow reservoir temperature range.
- At a reduced temperature range (and other conditions the same), the flow paths next to the main streamline now have a temperature closer to that of the main streamline. The same streamlines have the same arrival time, but tracers with lower thresholds, corresponding to the streamline max temperature, will dominate. In total, the streamlines with the same arrival times obtain threshold temperatures closer to the main streamline, i.e. a sharper curve.
- The effects of thermal anomalies (existence and locations) and inclined zones (conductivity and orientation) in the reservoir can be more easily observed when the injection-production position is non-horizontal as the tracer data become more sensitive to the orientation and location of such features.

In practice, forward simulations are required to match the breakthrough data from the field tests. Although it provides useful insights into the effects of geological and thermal heterogeneities on the tracer breakthrough data, a precise estimation of these unknowns relies on inverse modelling which uses model sensitivities to update parameters to be more consistent with observations. Our results show clear responses to geological and thermal heterogeneities which are clearly detectable when choosing a non-horizontal injection-production location.

The conclusions of this work are not limited to fractured reservoirs but can also applied to other types of geothermal reservoirs. During the entire lifecycle of geothermal reservoir exploitation, temperature-reporting tracer tests can be conducted to detect temperature range and reservoir thermal drawdown in the reservoir as well as other geological and thermal heterogeneities. At the exploration stage, the initial in-situ reservoir temperature information can be characterized quickly by the tracer curve using high flow rates, especially if shallow injection-production positions are chosen and the tracer can sweep the entire reservoir. For the production stage, the thermal drawdown status can be periodically quantified by comparison of the present temperatures to the initial ones. Potential challenges or limitations that one might be faced with when implementing our proposed approach in a realistic fractured geothermal reservoir scenario include injection-production configurations for inferring the temperature range, and uncertainties in the properties of liquid solution.

In addition to the investigations discussed in this work, the robustness of our proposed analysis approach has also been verified by simulations that consider the variations of communication between the inner reservoir and outer reservoir, injection and production rate and conversion degree of nanotracers. Nevertheless, the following aspects still deserve further studies:

- The impact of complex geometries which may include additional fractures and randomly distributed geological heterogeneities on the temperature-reporting nanotracer's behaviour in the reservoir and analysis curves.
- Use field test data to validate simulation results to ensure the practical applicability of this research work and its findings.
- Consider the impact of nanotracer properties and mechanisms such as gravity segregation, deposition and aggregation on the results predicted by the proposed numerical model.
- Incorporate the impact of potential fluid source (supply) and/or sink (leakage) from neighbouring geological strata.

## Acknowledgments

This study is part of the subtopic “Geoenergy” in the program “MTET - Materials and Technologies for the Energy Transition” of the Helmholtz Association. The support from the program is gratefully acknowledged. G.Y. is also funded by the China Scholarship Council (Grant No. 201709370076). P.Ø.A. acknowledges the Research Council of Norway and the industry partners of NCS2030 – RCN project number 331644 – for their support.

## References

Alaskar, M., Ames, M., Liu, C., Connor, S., Horne, R., Li, K., & Cui, Y. (2011). Smart nanosensors for in-situ temperature measurement in fractured geothermal reservoirs. *Annual Meeting of the Geothermal Resources Council*, San Diego, California, 15.

Alaskar, M., Ames, M., Liu, C., Li, K., & Horne, R. (2015). Temperature nanotracers for fractured reservoirs characterization. *Journal of Petroleum Science and Engineering*, *127*, 212–228. https://doi.org/10.1016/j.petrol.2015.01.021

Ames, M., Li, K., & Horne, R. (2015). The utility of threshold reactive tracers for characterizing temperature distributions in geothermal reservoirs. *Mathematical Geosciences*, *47*(1), 51–62. https://doi.org/10.1007/s11004-013-9506-x

Axelsson, G., Flovenz, O. G., Hauksdottir, S., Hjartarson, A., & Liu, J. (2001). Analysis of tracer test data, and injection-induced cooling, in the Laugaland geothermal field, N-Iceland. *Geothermics*, *30*(6), 697–725. https://doi.org/10.1016/S0375-6505(01)00026-8

Aydin, H., Nagabandi, N., Jamal, D., & Temizel, C. (2022). A Comprehensive Review of Tracer Test Applications in Geothermal Reservoirs. In *Day 2 Wed, April 27, 2022*. SPE. https://doi.org/10.2118/209325-MS

Bächler, D., Kohl, T., & Rybach, L. (2003). Impact of graben-parallel faults on hydrothermal convection—Rhine Graben case study. *Physics and Chemistry of the Earth*, *Parts A/B/C*, *28*(9-11), 431–441. https://doi.org/10.1016/S1474-7065(03)00063-9

Baillieux, P., Schill, E., Edel, J.-B., & Mauri, G. (2013). Localization of temperature anomalies in the Upper Rhine Graben: insights from geophysics and neotectonic activity. *International Geology Review*, *55*(14), 1744–1762. https://doi.org/10.1080/00206814.2013.794914

Cacace, M., & Jacquey, A. B. (2017). Flexible parallel implicit modelling of coupled thermal–hydraulic–mechanical processes in fractured rocks. *Solid Earth*, *8*(5), 921–941. https://doi.org/10.5194/se-8-921-2017

Cheng, A. H.-D., Ghassemi, A., & Detournay, E. (2001). Integral equation solution of heat extraction from a fracture in hot dry rock. *International Journal for Numerical and Analytical Methods in Geomechanics*, *25*(13), 1327–1338. https://doi.org/10.1002/nag.182

Cheng, P. (1979). Heat transfer in geothermal systems. In *Advances in Heat Transfer*. *Advances in Heat Transfer Volume 14* (Vol. 14, pp. 1–105). Elsevier. https://doi.org/10.1016/S0065-2717(08)70085-6

Cherubini, Y., Cacace, M., Blöcher, G., & Scheck-Wenderoth, M. (2013). Impact of single inclined faults on the fluid flow and heat transport: results from 3-D finite element simulations. *Environmental Earth Sciences*, *70*(8), 3603–3618. https://doi.org/10.1007/s12665-012-2212-z

Dashti, A., Gholami Korzani, M., Geuzaine, C., Egert, R., & Kohl, T. (2023). Impact of structural uncertainty on tracer test design in faulted geothermal reservoirs. *Geothermics*, *107*, 102607. https://doi.org/10.1016/j.geothermics.2022.102607

Dean, C., Reimus, P., Newell, D., Diagnostics, C., Observations, E. S., & Alamos, L. (Eds.) 2012. *Evaluation of a cation exchanging tracer to interrogate fracture surface area in EGS systems*. : Vol. *30*.

Divine, C. E., & McDonnell, J. J. (2005). The future of applied tracers in hydrogeology. *Hydrogeology Journal*, *13*(1), 255–258. https://doi.org/10.1007/s10040-004-0416-3

Domra Kana, J., Djongyang, N., Raïdandi, D., Njandjock Nouck, P., & Dadjé, A. (2015). A review of geophysical methods for geothermal exploration. *Renewable and Sustainable Energy Reviews*, *44*, 87–95. https://doi.org/10.1016/j.rser.2014.12.026

Egert, R., Korzani, M. G., Held, S., & Kohl, T. (2020). Implications on large-scale flow of the fractured EGS reservoir Soultz inferred from hydraulic data and tracer experiments. *Geothermics*, *84*, 101749. https://doi.org/10.1016/j.geothermics.2019.101749

Emry, E. L., Nyblade, A. A., Horton, A., Hansen, S. E., Julià, J., & Aster, R. C., et al. (2020). Prominent thermal anomalies in the mantle transition zone beneath the Transantarctic Mountains. *Geology*, *48*(7), 748–752. https://doi.org/10.1130/G47346.1

Erol, S., Bayer, P., Akın, T., & Akın, S. (2022). Advanced workflow for multi-well tracer test analysis in a geothermal reservoir. *Geothermics, 101*, 102375. https://doi.org/10.1016/j.geothermics.2022.102375

Fournier, R. O., & Rowe, J. J. (1966). Estimation of underground temperatures from the silica content of water from hot springs and wet-steam wells. *American Journal of Science*, *264*(9), 685–697. https://doi.org/10.2475/ajs.264.9.685

Fox, D. B., Koch, D. L., & Tester, J. W. (2016). An analytical thermohydraulic model for discretely fractured geothermal reservoirs. *Water Resources Research*, *52*(9), 6792–6817. https://doi.org/10.1002/2016WR018666

France, W. D., Vericella, J., Duoss, E., Smith, M., Aines, R., & Roberts, J. (2014). *Smart tracers for geothermal reservoir assessment.*

Frey, M., Bär, K., Stober, I., Reinecker, J., van der Vaart, J., & Sass, I. (2022). Assessment of deep geothermal research and development in the Upper Rhine Graben. *Geothermal Energy*, *10*(1). https://doi.org/10.1186/s40517-022-00226-2

Geuzaine, C., & Remacle, J.-F. (2009). Gmsh: A 3‐D finite element mesh generator with built‐in pre‐ and post‐processing facilities. *International Journal for Numerical Methods in Engineering*, *79*(11), 1309–1331. https://doi.org/10.1002/nme.2579

Gringarten, A. C., Witherspoon, P. A., & Ohnishi, Y. (1975). Theory of heat extraction from fractured hot dry rock. *Journal of Geophysical Research*, *80*(8), 1120–1124. https://doi.org/10.1029/JB080i008p01120

Hawkins, A. J., Becker, M. W., & Tester, J. W. (2018). Inert and adsorptive tracer tests for field measurement of flow‐wetted surface area. *Water Resources Research*, *54*(8), 5341–5358. https://doi.org/10.1029/2017WR021910

Hawkins, A. J., Bender, J. T., Grooms, R. D., Schissel, C. J., & Tester, J. W. (2021). Temperature-responsive smart tracers for field-measurement of inter-well thermal evolution: Heterogeneous kinetics and field demonstration. *Geothermics*, *92*, 102046. https://doi.org/10.1016/j.geothermics.2021.102046

Kohl, T., & Rybach, L. (1996). Thermal and hydraulic aspects of the KTB drill site. *Geophysical Journal International*, *124*(3), 756–772. https://doi.org/10.1111/j.1365-246X.1996.tb05636.x

Kong, X.-Z., Deuber, C. A., Kittilä, A., Somogyvári, M., Mikutis, G., & Bayer, P., et al. (2018). Tomographic Reservoir Imaging with DNA-Labeled Silica Nanotracers: The First Field Validation. *Environmental Science & Technology*, *52*(23), 13681–13689. https://doi.org/10.1021/acs.est.8b04367

Leecaster, K., Ayling, B., Moffitt, G., & Rose, P. (2012). Use of safranin T as a reactive tracer for geothermal reservoir characterization. *37th Workshop on Geothermal Reservoir Engineering*. Retrieved from https://pangea.stanford.edu/ERE/pdf/IGAstandard/SGW/2012/Leecaster.pdf

Li, J., Pei, Y., Jiang, H., Zhao, L., Li, L., & Zhou, H., et al. (2016). Tracer flowback based fracture network characterization in hydraulic fracturing. In *Day 2 Tue, November 08, 2016*. SPE. https://doi.org/10.2118/183444-MS

Li, L., Jiang, H., Li, J., Wu, K., Meng, F., & Chen, Z. (2017). Modeling tracer flowback in tight oil reservoirs with complex fracture networks. *Journal of Petroleum Science and Engineering*, *157*, 1007–1020. https://doi.org/10.1016/j.petrol.2017.08.022

Lu, C., Jiang, H., You, C., Wang, Y., Ma, K., & Li, J. (2021). A novel method to determine the thief zones in heavy oil reservoirs based on convolutional neural network. *Journal of Petroleum Science and Engineering*, *201*, 108471. https://doi.org/10.1016/j.petrol.2021.108471

Lu, S.-M. (2018). A global review of enhanced geothermal system (EGS). *Renewable and Sustainable Energy Reviews*, *81*, 2902–2921. https://doi.org/10.1016/j.rser.2017.06.097

Lund, J. W., Bjelm, L., Bloomquist, G., & Mortensen, A. K. (2008). Characteristics, development and utilization of geothermal resources – a Nordic perspective. *Episodes*, *31*(1), 140–147. https://doi.org/10.18814/epiiugs/2008/v31i1/019

Moeck, I. S. (2014). Catalog of geothermal play types based on geologic controls. *Renewable and Sustainable Energy Reviews*, *37*, 867–882. https://doi.org/10.1016/j.rser.2014.05.032

Nitschke, F., Held, S., Villalon, I., Neumann, T., & Kohl, T. (2017). Assessment of performance and parameter sensitivity of multicomponent geothermometry applied to a medium enthalpy geothermal system. *Geothermal Energy*, *5*(1). https://doi.org/10.1186/s40517-017-0070-3

Nottebohm, M., Licha, T., & Sauter, M. (2012). Tracer design for tracking thermal fronts in geothermal reservoirs. *Geothermics*, *43*, 37–44. https://doi.org/10.1016/j.geothermics.2012.02.002

Olasolo, P., Juárez, M. C., Morales, M. P., D´Amico, S., & Liarte, I. A. (2016). Enhanced geothermal systems (EGS): A review. *Renewable and Sustainable Energy Reviews*, *56*, 133–144. https://doi.org/10.1016/j.rser.2015.11.031

Permann, C. J., Gaston, D. R., Andrš, D., Carlsen, R. W., Kong, F., & Lindsay, A. D., et al. (2020). MOOSE: Enabling massively parallel multiphysics simulation. *SoftwareX*, *11*, 100430. https://doi.org/10.1016/j.softx.2020.100430

Plummer, M. A., Palmer, C. D., Hull, L. C., & Mattson, E. D. (2010). Sensitivity of a reactive-tracer based estimate of thermal breakthrough in an EGS to properties of the reservoir and tracer. *Idaho National Lab. (INL), Idaho Falls, ID (United States)*, 1–8. Retrieved from https://pangea.stanford.edu/ERE/pdf/IGAstandard/SGW/2012/Plummer.pdf

Plummer, M. A., Palmer, C. D., Mattson, E. D., & Hull, L. C. (2011). A reactive tracer analysis method for monitoring thermal drawdown in geothermal reservoirs. *36th Workshop on Geothermal Reservoir Engineering*, 5. Retrieved from https://pangea.stanford.edu/ERE/pdf/IGAstandard/SGW/2011/palmer.pdf

Pollack, A., Cladouhos, T. T., Swyer, M. W., Siler, D., Mukerji, T., & Horne, R. N. (2021). Stochastic inversion of gravity, magnetic, tracer, lithology, and fault data for geologically realistic structural models: Patua Geothermal Field case study. *Geothermics*, *95*, 102129. https://doi.org/10.1016/j.geothermics.2021.102129

Puddu, M., Mikutis, G., Stark, W. J., & Grass, R. N. (2016). Submicrometer-Sized Thermometer Particles Exploiting Selective Nucleic Acid Stability. *Small (Weinheim an Der Bergstrasse, Germany)*, *12*(4), 452–456. https://doi.org/10.1002/smll.201502883

Qiao, Y., Andersen, P., Evje, S., & Standnes, D. C. (2018). A mixture theory approach to model co- and counter-current two-phase flow in porous media accounting for viscous coupling. *Advances in Water Resources*, *112*, 170–188. https://doi.org/10.1016/j.advwatres.2017.12.016

Redden, G., Stone, M., Wright, K. E., Mattson, E., Palmer, C. D., & Rollins, H., et al. (2010). Tracers for characterizing enhanced geothermal systems. *Proceedings of Thirty-Fifth Workshop on Geothermal Reservoir Engineering*.

Robinson, B. A. (1985). *Tracer and Geochemistry Analysis – Experiment 2059.*

Robinson, B. A., & Tester, J. W. (1984). Dispersed fluid flow in fractured reservoirs: An analysis of tracer ‐ determined residence time distributions. *Journal of Geophysical Research*, *89*(B12), 10374–10384. https://doi.org/10.1029/JB089iB12p10374

Robinson, B. A., Tester, J. W., & Brown, L. F. (1988). Reservoir sizing using inert and chemically reacting tracers. *SPE Formation Evaluation*, *3*(01), 227–234. https://doi.org/10.2118/13147-PA

Rose, P. E. (1994). The application of rhodamine WT as a geothermal tracer. *Geothermal Resources Council Transactions*, *18*, 237–240.

Rudolph, B., Berson, J., Held, S., Nitschke, F., Wenzel, F., Kohl, T., & Schimmel, T. (2020). Development of thermo-reporting nanoparticles for accurate sensing of geothermal reservoir conditions. *Scientific Reports*, *10*(1), 11422. https://doi.org/10.1038/s41598-020-68122-y

Sanjuan, B., Millot, R., Ásmundsson, R., Brach, M., & Giroud, N. (2014). Use of two new Na/Li geothermometric relationships for geothermal fluids in volcanic environments. *Chemical Geology*, *389*, 60–81. https://doi.org/10.1016/j.chemgeo.2014.09.011

Sanjuan, B., Pinault, J.-L., Rose, P., Gérard, A., Brach, M., & Braibant, G., et al. (2006). Tracer testing of the geothermal heat exchanger at Soultz-sous-Forêts (France) between 2000 and 2005. *Geothermics*, *35*(5-6), 622–653. https://doi.org/10.1016/j.geothermics.2006.09.007

Shan, C., & Pruess, K. (2005). An analytical solution for slug tracer tests in fractured reservoirs. *Water Resources Research*, *41*(8). https://doi.org/10.1029/2005WR004081

Smith, L., & Chapman, D. S. (1983). On the thermal effects of groundwater flow: 1. Regional scale systems. *Journal of Geophysical Research*, *88*(B1), 593–608. https://doi.org/10.1029/JB088iB01p00593

Tang, Y., Ma, T., Chen, P., & Ranjith, P. G. (2020). An analytical model for heat extraction through multi-link fractures of the enhanced geothermal system. *Geomechanics and Geophysics for Geo-Energy and Geo-Resources*, *6*(1). https://doi.org/10.1007/s40948-019-00123-2

Tester, J. W., Brown, D. W., & Potter, R. M. (1989). Hot Dry Rock geothermal energy---A new energy agenda for the twenty-first century, 1–36. Retrieved from https://doi.org/10.2172/5620783

Tester, J. W., Robinson, B. A., & Ferguson, J. (1987). The theory and selection of chemically reactive tracers for reservoir thermal capacity production, 1–12. Retrieved from https://www.osti.gov/biblio/888538

Vitorge, E., Szenknect, S., Martins, J. M.-F., Barthès, V., & Gaudet, J.-P. (2014). Comparison of three labeled silica nanoparticles used as tracers in transport experiments in porous media. Part II: transport experiments and modeling. *Environmental Pollution (Barking, Essex : 1987)*, *184*, 613–619. https://doi.org/10.1016/j.envpol.2013.08.016

Wilkins, A., Green, C. P., & Ennis-King, J. (2021). An open-source multiphysics simulation code for coupled problems in porous media. *Computers & Geosciences*, *154*, 104820. https://doi.org/10.1016/j.cageo.2021.104820

Williams, M. D., Reimus, P., Vermeul, V. R., Rose, P., Dean, C. A., & Watson, T. B., et al. (2013). Development of models to simulate tracer tests for characterization of enhanced geothermal systems, 1–118. https://doi.org/10.2172/1083416

Williams, M. D., Vermeul, V. R., Reimus, P. W., Newell, D., & Watson, T. B. (2010). Development of models to simulate tracer behavior in enhanced geothermal systems, 1–44. https://doi.org/10.2172/992377

Xu, T., Liang, X., Xia, Y., Jiang, Z., & Gherardi, F. (2022). Performance evaluation of the Habanero enhanced geothermal system, Australia: Optimization based on tracer and induced micro-seismicity data. *Renewable Energy*, *181*, 1197–1208. https://doi.org/10.1016/j.renene.2021.09.111

Yan, G., Busch, B., Egert, R., Esmaeilpour, M., Stricker, K., & Kohl, T. (2023). Transport mechanisms of hydrothermal convection in faulted tight sandstones. *Solid Earth*, *14*(3), 293–310. https://doi.org/10.5194/se-14-293-2023

Ystroem, L. H., Nitschke, F., Held, S., & Kohl, T. (2020). A multicomponent geothermometer for high-temperature basalt settings. *Geothermal Energy*, *8*(1). https://doi.org/10.1186/s40517-020-0158-z

## Appendix I: Fully Coupled Processes of Fluid Flow, Heat Transfer, Transport and Reaction for Temperature-reporting Nanoparticle Tracers

### (a) Detailed Equations of Fully Coupled Processes

Equation 4 indicates a sharp conversion process of the injected nanotracers / reactants into products. To release this constraint, we include a conversion factor $Z$ in the following reaction expression for temperature-reporting nanotracers:

$$(C_{T_{thre.}}^{reac.\,n})^{updated} = Z^n \cdot C_{T_{thre.}}^{reac.\,n} \tag{A1}$$

where $(C_{T_{thre.}}^{reac.\,n})^{updated}$ represents the newly updated concentration of the reactant after reaction (at time step $n$) and $Z$ is defined as:

$$Z^n = \begin{cases} 1, & T^n < (T_{thre.} - a); \\ \frac{1}{1+e^{b\cdot(T^n - T_{thre.})}}, & (T_{thre.} - a) \le T^n \le (T_{thre.} + a); \\ 0, & T^n > (T_{thre.} + a). \end{cases} \tag{A2}$$

where $a$ (°C) and $b$ (=6/$a$, °C$^{-1}$) are conversion constants that can be controlled such that a smooth conversion between 100% and 0% nanotracer conversion can be achieved when environment temperature $T$ is near the nanotracer temperature threshold $T_{thre.}$.

The product concentration after the reaction at the time step $n$ is updated with:

$$(C_{T_{thre.}}^{prod.\,n})^{updated} = (1 - Z^n) \cdot C_{T_{thre.}}^{reac.\,n} + C_{T_{thre.}}^{prod.\,n} \tag{A3}$$

where the two parts on the right side separately refer to the concentration increase of the product after the reaction and product concentration at time step $n$.

The updated results $(C_{T_{thre.}}^{reac.\,n})^{updated}$ and $(C_{T_{thre.}}^{prod.\,n})^{updated}$ at time step *n* are separately used explicitly in the following tracer transport Equations A4 and A5 for the implicit computation of the reactant and product concentrations at time step *n*+1.

$$\frac{C_{T_{thre.}}^{reac.\,n+1} - (C_{T_{thre.}}^{reac.\,n})^{updated}}{\Delta t} - \nabla \cdot \left(\boldsymbol{D} \nabla C_{T_{thre.}}^{reac.\,n+1}\right) + \nabla \cdot \left(\boldsymbol{u}_{\boldsymbol{w}}^{\boldsymbol{n+1}} C_{T_{thre.}}^{reac.\,n+1}\right) - Q_{C_{T_{thre.}}^{reac.\,n+1}} = 0 \tag{A4}$$

$$\frac{C_{T_{thre.}}^{prod.\,n+1} - (C_{T_{thre.}}^{prod.\,n})^{updated}}{\Delta t} - \nabla \cdot \left(\boldsymbol{D} \nabla C_{T_{thre.}}^{prod.\,n+1}\right) + \nabla \cdot \left(\boldsymbol{u}_{\boldsymbol{w}}^{\boldsymbol{n+1}} C_{T_{thre.}}^{prod.\,n+1}\right) - Q_{C_{T_{thre.}}^{prod.\,n+1}} = 0 \tag{A5}$$

After obtaining $C_{T_{thre.}}^{reac.\,n+1}$ and $C_{T_{thre.}}^{prod.\,n+1}$, we need to update these two variables at time step *n+1* according to the new conversion factor $Z^{n+1}$ using Equations A1 and A3.

### (b) Numerical Algorithms of the Fully Coupled Processes

The numerical algorithms of the fully coupled processes of fluid flow, heat transfer, transport and reaction for temperature-reporting nanoparticle tracers are shown in Figure A1. At time step *n*, the fluid flow model, nanotracer transport model together with heat transfer model are solved implicitly. After obtaining the results, the reactant and product concentrations of tracers are updated using the nanotracer reaction model, which provides the inputs for the tracer computation at next time step *n*+1.

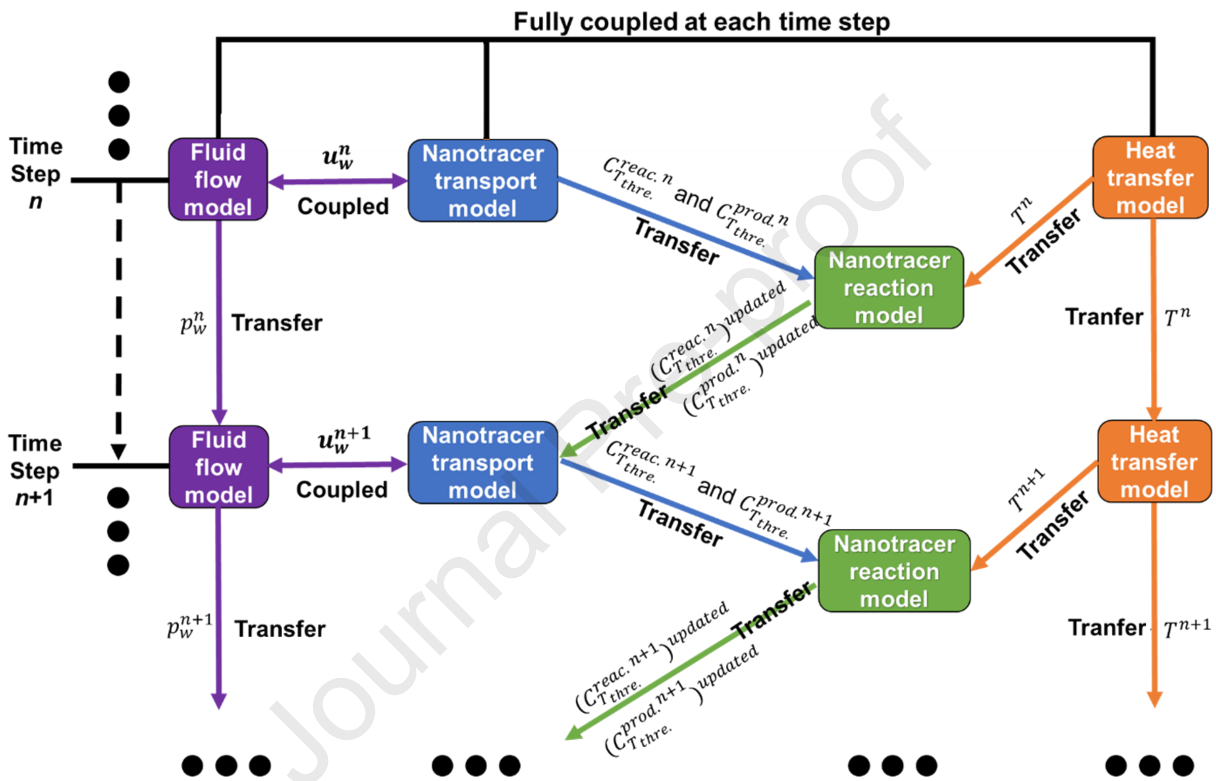


**Figure A1. Schematic of the fully coupled fluid flow, heat transfer, transport and reaction models of temperature-reporting nanoparticle tracers.**

## Appendix II: Numerical Model Validation

A one-dimensional (1D) simulation is run to validate the numerical model with coupled fluid flow, heat transfer, transport and reaction for temperature-reporting nanoparticle tracers, shown in Figure A2. The numerical results produced by the PorousFlow module (Wilkins et al., 2021) within the MOOSE framework (Permann et al., 2020) are validated against an analytical solution. The analytical solution is simply a stepwise function, which satisfies the mass conservation law and chemical conversion.

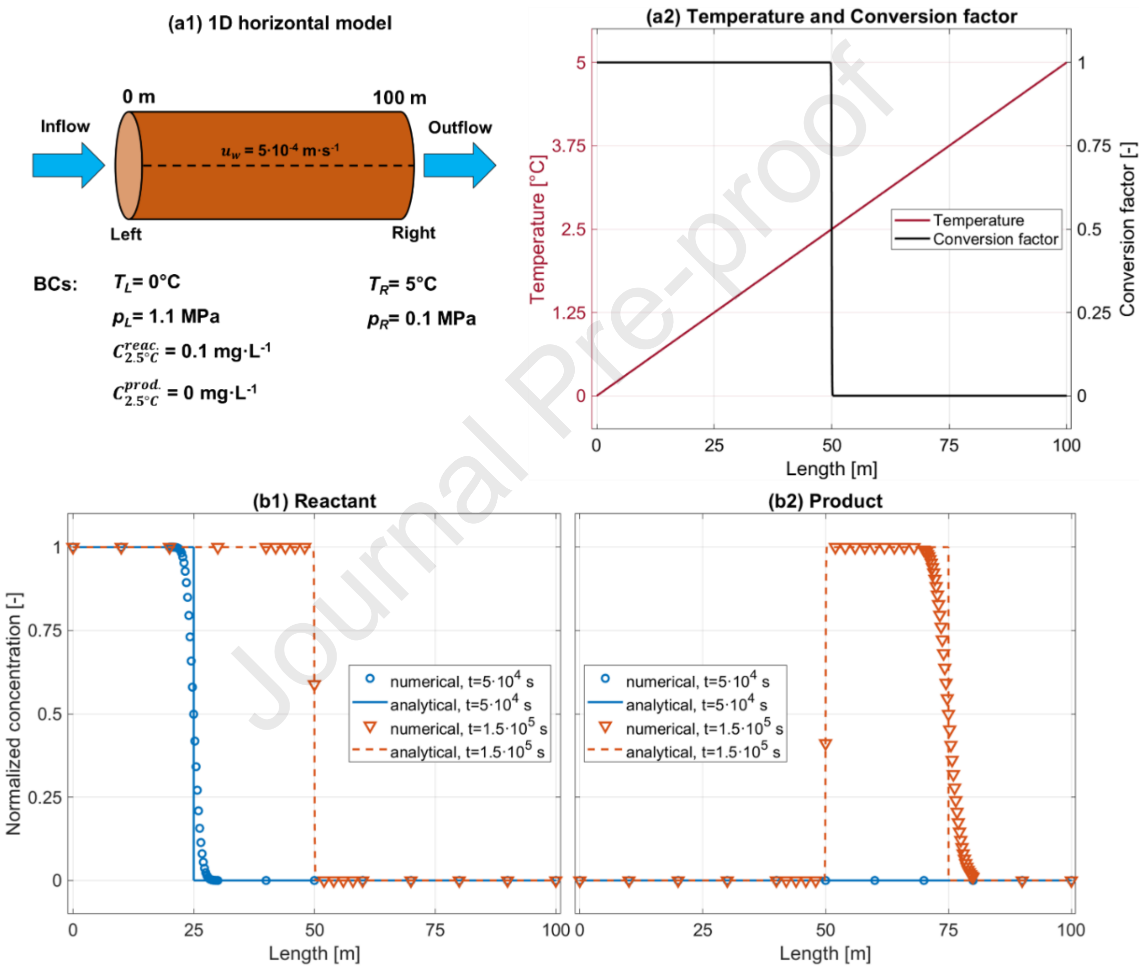


**Figure A2. Validation on the fully coupled processes of fluid flow, heat transfer, transport and reaction for temperature-reporting nanoparticle tracers: (a1) 1D model with boundary conditions; (a2) temperature and conversion factor profiles; (a3, a4) comparison of numerical and analytical results for reactant $C^{reac.}_{T_{2.5°C}}$ and product $C^{prod.}_{T_{2.5°C}}$ at $5{\cdot}10^4$ s and $1.5{\cdot}10^5$ s.**

As shown in Figure A2 (a1), incompressible fluid is injected with a nanotracer reactant (threshold 2.5°C) into a 100-meter horizontal system. The Darcy velocity is $5{\cdot}10^{-4}$ m·s$^{-1}$ and the injected nanotracer reactant concentration is 0.1 mg·L$^{-1}$. The porosity is assumed 1 and fluid properties are set constant (density 1000 kg·m$^{-3}$, viscosity $10^{-3}$ Pa·s and thermal conductivity 0.6

$W\cdot m^{-1}\cdot k^{-1}$). The system temperature (0°C~5°C) and pressure (1.1 MPa~0.1 MPa) distributions are constrained following a linear relation from inlet to outlet, during the whole process.

The temperature distribution and the corresponding conversion factor *Z* along the model are shown in Figure A2 (a2). The comparisons between the analytical and numerical solutions show agreement for both reactant and product at the two selected times $5\cdot10^4$ s and $1.5\cdot10^5$ s.

## Appendix III: Mesh Sensitivity Analysis

To illustrate the convergence of the chosen discretization, a comparison of the conservative tracer breakthrough curves at the production well is provided in Figure A3 for three different meshes. The curves are practically indistinguishable when the element number reaches 331’799. Consequently, the simulations reported in this study are performed with 331’799 elements.

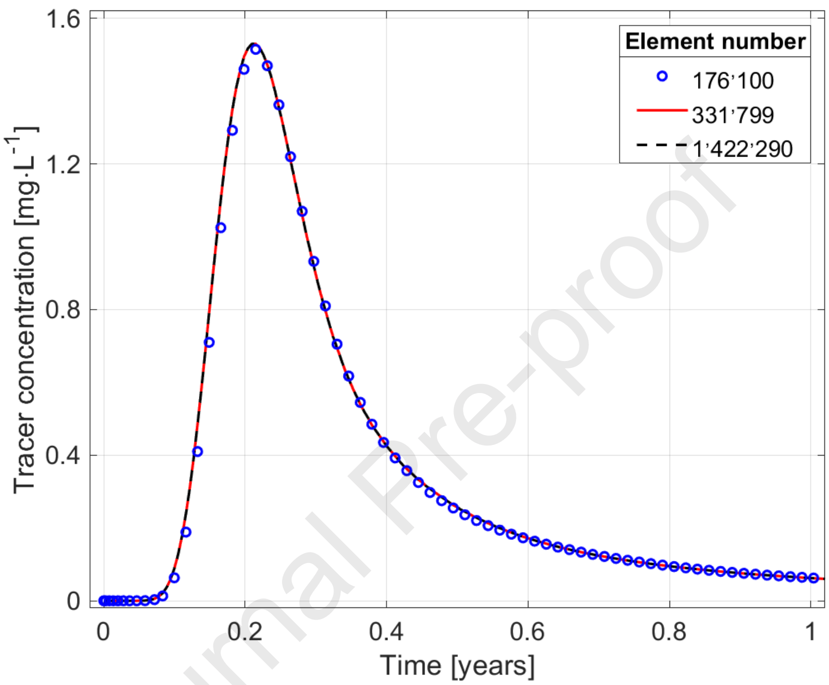


**Figure A3. Comparison of conservative tracer breakthrough curves for different element numbers.**

**Highlights**

- Temperature-reporting nanoparticle tracer tests are numerically implemented in a three-dimensional fractured geothermal reservoir.
- The working mechanisms of the temperature-reporting nanoparticle tracers are illustrated through field simulations using a proposed modeling approach.
- Our proposed analysis curves can provide responses to the reservoir temperature distribution as well as geological and thermal heterogeneities based on the tracer breakthrough data.

**Declaration of interests**

☐ The authors declare that they have no known competing financial interests or personal relationships that could have appeared to influence the work reported in this paper.

☒ The authors declare the following financial interests/personal relationships which may be considered as potential competing interests:

| |
|---|
| Guoqiang Yan reports financial support was provided by China Scholarship Council. If there are other authors, they declare that they have no known competing financial interests or personal relationships that could have appeared to influence the work reported in this paper. |